Constraining the initial entropy of directly-detected exoplanets

G.-D. Marleau[1,2]* and A. Cumming[2]*

[1]*Max-Planck-Institut für Astronomie, Königstuhl 17, D-69117 Heidelberg, Germany*
[2]*Department of Physics, McGill University, 3600 rue University, Montréal, Québec H3A 2T8, Canada*

11 February 2013

ABSTRACT

The initial entropy S_i of a gas giant planet is a key witness to its formation history and a crucial quantity for its early evolution. However, formation models are not yet able to reliably predict S_i, making an observational determination of initial entropies essential in order to guide formation scenarios. Using a grid of models in mass and entropy, we show how to place joint constraints on the mass and initial entropy of an object from its observed luminosity and age. Moreover, we demonstrate that with mass information, e.g. from dynamical stability analyses or radial velocity, tighter bounds can be set on the initial entropy. We apply this procedure to 2M1207 b and find that its initial entropy is at least 9.2 k_B/baryon, assuming that it does not burn deuterium. For the planets of the HR 8799 system, we infer that they must have formed with $S_i > 9.2$ k_B/baryon, independent of the age uncertainties for the star. Finally, a similar analysis for β Pic b reveals that it must have formed with $S_i > 10.5$ k_B/baryon, using the radial-velocity mass upper limit. These initial entropy values are respectively ca. 0.7, 0.5, and 1.5 k_B/baryon higher than the ones obtained from core accretion models by Marley et al., thereby *quantitatively* ruling out the coldest starts for these objects and constraining warm starts, especially for β Pic b.

Key words: planets and satellites: general – methods: analytical – techniques: imaging spectroscopy – stars: individual: 2MASSWJ 1207334–393254 – stars: individual: HR 8799 – stars: individual: β Pictoris.

1 INTRODUCTION

While only a handful of directly-detected exoplanets is currently known, the near future should bring a statistically significant sample of directly-imaged exoplanets, thanks to a number of surveys underway or coming online soon. Examples include VLT/SPHERE, Gemini/GPI, Subaru/HiCIAO, Hale/P1640 (Vigan et al. 2010; Chauvin et al. 2010; Liu et al. 2010; McBride et al. 2011; McElwain et al. 2012; Hinkley et al. 2011b) An important input for predicting the yields of such surveys and for interpreting their results is the cooling history of gas giant planets. In the traditional approach Stevenson (1982); Burrows et al. (1997); Baraffe et al. (2003), objects begin their cooling, fully formed, with an arbitrarily high (specific) entropy and hence radius and luminosity. In the past, the precise choice of initial conditions has been of no consequence because only the 4.5-Gyr-old Solar System's gas giants were known, while the high initial entropy is forgotten on the short Kelvin–Helmholtz timescale GM^2/RL (Stevenson 1982; Marley et al. 2007). However, direct-detection surveys are aiming specifically at young ($\leqslant 500$ Myr) systems, and the traditional models, as their authors explicitly recognised, are not reliable at early ages.

Using the standard core-accretion formation model

(Pollack et al. 1996; Bodenheimer et al. 2000; Hubickyj et al. 2005), Marley et al. (2007, hereafter M07) found that newly-formed gas giants produced by core accretion should be substantially colder than the usual cooling tracks that begin with arbitrarily hot initial conditions assume. These outcomes are known as 'cold start' and 'hot start', respectively. M07 however noted that there are a number of assumptions and approximations that go into the core accretion models that make the predicted entropy uncertain. In particular, the accretion shock at the surface of the planet is suspected to play a key role as most of the mass is processed through it (M07; Baraffe, Chabrier, & Barman 2010) but there does not yet exist a satisfactory treatment of it. Furthermore, there may also be an accretion shock in the other main formation scenario, gravitational instability, such that it too could yield cooler planets than usually expected (see section 8 of Mordasini et al. 2012b).

The most reasonable viewpoint for now is therefore to consider that the initial entropy is highly uncertain and may lie almost anywhere between the cold values of M07 and the hot starts. In fact, M07 calculated 'warm start' models that were intermediate between the cold and hot starts, and recently, Spiegel & Burrows (2012) calculated cooling tracks and spectra of giant planets beginning with a range of initial entropies. This uncertainty in the initial entropy means that observations are in a privileged position to inform models of planet formation, for which the initial entropy (or

* E-mail: marleau@mpia.de, cumming@physics.mcgill.ca

luminosity) is an easily accessible output. Its determination both on an individual basis as well as for a statistically meaningful sample of planets would be very valuable, with the latter allowing quantitative comparisons to planet population synthesis (Ida & Lin 2004; Mordasini et al. 2012b,a). Contrasting with the current small number of direct detections, which almost exclusively consist of massive objects on wide orbits, the near future should bring both qualitative and quantitative changes to the collection of known ones. Indeed, upcoming and ongoing surveys such as SPHERE, GPI, Hi-CIAO, JWST are expected to reveal a number of light objects at small separations from their parent star (i.e. Jupiter-like planets) It is therefore crucial to highlight now the need to interpret direct observations in a model-independent fashion and to think about information these yield about the initial conditions of gas giants.

In this paper, we investigate the constraints on the mass M and initial entropy S_i that come from a luminosity and age determination of a directly-detected object, focussing on exoplanets. Since the current luminosity increases both with M and with S_i, these constraints take the form of a 'trade-off curve' between M and S_i. We show that, in the planetary regime, the allowed values of M and S_i can be divided into two regions. The first is a hot-start region where the initial entropy can be arbitrarily high but where the mass is well determined. This corresponds to the usual mass determination by fitting hot-start cooling curves. The second corresponds to solutions with a lower, tightly-constrained initial entropy for which the planet mass has to be larger than the hot-start mass. For masses above the deuterium-burning limit, the required entropies drop more steeply with increasing mass due to energy injection by deuterium burning, but we defer a discussion of this to a forthcoming paper. The degeneracy between mass and initial entropy means that in general the mass and entropy cannot be constrained independently from a measurement of luminosity alone. When additional mass information are available, for example for multiple-planet systems or systems with radial velocity, it is possible to constrain the formation entropy more tightly.

We start in Section 2 by describing our gas-giant cooling models, discussing the luminosity scalings with mass and entropy, and comparing to previous calculations in the literature. In Section 3, we show in general how to derive constraints on the mass and initial entropy of a directly-detected exoplanet by comparing its measured luminosity and age to cooling curves with a range of initial entropies. We briefly consider in Section 4 similar constraints based on a (spectral) determination of the effective temperature and surface gravity. We apply the procedure based on bolometric luminosities in Section 5 to three particularly interesting systems – 2M1207, HR 8799, and β Pictoris – and derive lower bounds on their initial entropies. For HR 8799 and β Pic, we use the available information on the masses to constrain the initial entropies more tightly. Finally, we offer a summary and concluding remarks in Section 6.

2   COOLING MODELS WITH ARBITRARY INITIAL ENTROPY

Given its importance in the initial stages of a planet's cooling, we focus in this paper on the internal entropy of a gas giant as a fundamental parameter which, along with its mass, determines its structure and controls its evolution. Very few authors have explicitly considered entropy as the second fundamental quantity even though this approach is more transparent than the usual, more intuitive use of time as the second independent variable. In this section, before comparing our models to standard ones, we discuss in-

terior temperature–pressure profiles and semi-analytically explain the different scalings of luminosity on mass and entropy which appear in the models.

2.1   Calculation of gas giant models

We calculate the evolution of cooling gas giants by a 'following the adiabats' approach (Hubbard 1977; Fortney & Hubbard 2004; Arras & Bildsten 2006). We generate a large grid of planet models with ranges of interior specific entropy S and mass M and determine for each model the luminosity $L = L(M, S)$ at the top of the convection zone. We then use it to calculate the rate of change of the convective zone's entropy dS/dt, which is defined by writing the entropy equation $\partial L/\partial m = -T \partial S/\partial t$ as

$$L = -\frac{dS}{dt} \int T \, dm + L_D, \tag{1}$$

with L_D the luminosity due to deuterium burning in the convection zone. The assumptions in this approach are that $\partial S/\partial t$ is constant throughout the convection zone and that no luminosity is generated in the atmosphere. For these to hold, we require both the thermal timescale $t_{therm}(r) = P c_P T/gF$ (Arras & Bildsten 2006) – where c_P is the specific heat capacity, g the gravity, and F the local flux – in the radiative zone overlying the convective core and the convective turnover[1] timescale to be much shorter than the timescale on which the entropy is changing, $t_S = -S/(dS/dt) = M\overline{T}S/L$, with $\overline{T}$ the mass-weighted mean temperature in the convection zone. A similar approach was used to study the evolution of ohmically-heated irradiated gas giants by Huang & Cumming (2012).

We do not include deuterium burning directly in the planet models since it always occurs inside the convection zone. Instead, we calculate the deuterium burning luminosity per unit deuterium mass fraction for each model in the grid and use it in equation (1) to follow the cooling of the planet and the time evolution of the deuterium mass fraction averaged over the convective region. We use the deuterium burning rate from Caughlan & Fowler (1988) and include the intermediate screening correction from Graboske et al. (1973), following Burrows & Liebert (1993). We adopt a standard initial D/H number ratio of 2×10^{-5} (i.e. a deuterium mass fraction $X_D = 3.0 \times 10^{-5}$). Since we focus here on directly-detected planets, we defer a detailed exploration of deuterium burning in our models to an ulterior publication. However, we may already mention that cooling curves starting at low entropy can exhibit an initial increase in their luminosity due to deuterium burning. We subsequently noticed that the colder starts in fig. 8 of Mollière & Mordasini (2012) show a similar behaviour.

To construct a model with a given mass M and internal entropy S, we integrate inwards from the photosphere and outwards from the center, adjusting the central pressure, the cooling time t_S, and the luminosity L and the radius R at the top of the inner zone until the two integrations match at a pressure of 30 kbar. We use the Eddington approximation at the photosphere, setting $T = T_{eff}$ at $P_{phot} = 2g/3\kappa$, and take the solar-metallicity (based on Lodders 2003) radiative opacity from Freedman, Marley, & Lodders (2008). In the deep interior, the contribution from the electron conductive opacity of Cassisi et al.

---

[1] We do make the standard assumption that the interior is fully convective, even though stabilising compositional gradients have been suggested to possibly shut off large-scale convective movements (Stevenson 1979; Leconte & Chabrier 2012).

(2007) is also included. The equation of state for the hydrogen–helium mixture is that of Saumon, Chabrier, & van Horn (1995, hereafter SCvH) with a helium mass fraction $Y = 0.25$. Since we focus on gas giants, we do not include a rocky core, which was found in a test grid to increase the luminosities by at most a few percent at the lower masses, as in Saumon et al. (1996).

The grid has a lower entropy limit of $S \simeq 7$–$7.5\ k_B$/baryon[2]. The upper S limit in the grid is set by the requirement that $R \lesssim 8\ R_J$, a value found to make numerical convergence straightforward. The upper limits are $S_{max} \simeq 12$ near $1\ M_J$ and $S_{max} \simeq 14$ for the higher masses.

Fig. 1 shows interior profiles in the T–P plane for a range of entropies and masses. Schematically, since hydrostatic balance dictates $P_c \sim M^2/R^4$, increasing the mass at a fixed entropy extends the centre to a higher pressure along the adiabat. This is exacerbated at high entropies, where the planet substantially shrinks with increasing mass (while low-entropy objects have a roughly constant radius). At fixed mass, increasing the entropy mostly shifts the centre to higher T or to lower P. The first case obtains for low-entropy objects, which are essentially at zero temperature in the sense that $k_B T_c \ll E_F$, where T_c is the central temperature and E_F the Fermi energy level at the centre. Increasing the entropy partially lifts the degeneracy since the degeneracy parameter $y = k_B T_c / E_F \propto T_c / \varrho_c^{2/3}$ is a monotonic function of S, and P_c remains constant because of the constant radius. At entropies higher than a turn-over value of $\simeq 10\ k_B$/baryon, the central temperature does not increase (and even decreases) with entropy. As for P_c, it decreases because the radius increases. These behaviours also hold at higher masses not shown in the figure.

As for the 1-M_J planet with $S = 9$ shown in Fig. 1, some models with entropy $S \simeq 8$–9.5 show a second, 'detached' convective zone at lower pressures, which follows from a re-increase of the Rosseland mean opacity (see section 3.1 of Burrows et al. 1997). This second convection zone, which is at most at an entropy $0.2\ k_B$/baryon higher than the convective core, will not affect the evolution of the object since the radiative thermal timescale is much shorter than the cooling time t_S, throughout the atmosphere. This holds in particular at the inner radiative-convective boundary (RCB); for example, the 1-M_J, $S = 10$ model has $t_S = 14$ Myr and $t_{therm} = 0.2$ Myr at its RCB. Finally, we note that the higher-entropy objects ($S \gtrsim 11.5$, with some dependence on mass) are convective from the centre all the way to the photosphere.

2.2 Luminosity as a function of mass and entropy

To provide a model-independent way of thinking about an object's brightness and thus to facilitate comparison with other models, we show in Fig. 2 the luminosity of the planet as a function of its internal entropy. We focus on objects without significant deuterium burning. Two main regimes are apparent: at lower entropies, the scaling with mass is roughly $L \sim M$, while at high entropies, the luminosity becomes almost insensitive to mass, i.e. $L \sim M^0$. Looking more closely, the high-luminosity regime is described by $L \propto M^{0.3}$ (for $M \gtrsim 1\ M_J$), and the brief flattening of the luminosity slope with entropy at $S \sim 8.2$–9, depending on mass, marks a transition from $L \propto M^1$ to $L \propto M^{0.7}$, respectively at fixed intermediate and low entropy.

---

[2] Entropy values in this work are always given in the usual units of multiples of Boltzmann's constant k_B per baryon (i.e. per mass of hydrogen atom). For comparison, 4.5-Gyr-old Jupiter currently has an entropy of 6.5.
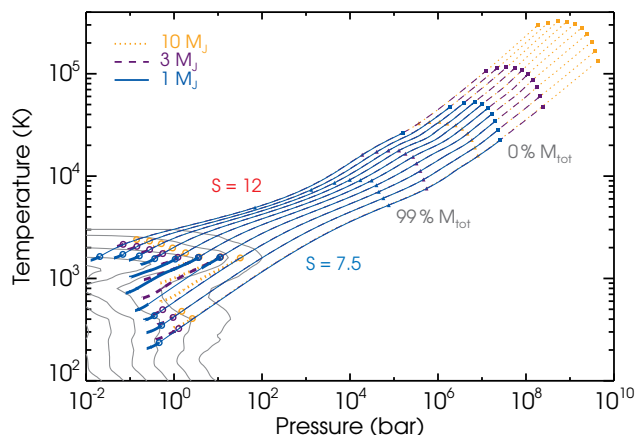

Figure 1. Temperature–pressure profiles of core-less planets with entropy $S = 7.5$–$12\ k_B$/baryon (bottom to top), in steps of $0.5\ k_B$/baryon, and $M = 1$, 3, and $10\ M_J$ (full, dashed, and dotted lines, respectively). The radii at $S = 7.5$, 8, 9, 10, 11, and $12\ k_B$/baryon are 1.12, 1.18, 1.34, 1.66, 2.48, and 7.94 R_J (1 M_J), 1.11, 1.16, 1.29, 1.52, 1.96, and 2.85 R_J (3 M_J), and 1.03, 1.07, 1.19, 1.40, 1.76, and 2.34 R_J (10 M_J), respectively. Squares indicate the centre and triangles mark where the enclosed mass is 99 per cent of the total mass for each model. Curves end at the photosphere in the Eddington approximation, and the thick part(s) of each curve show the radiative zone(s), while the thin part(s) of the curve are convective; the radiative-convective boundary relevant for the thermal evolution is highlighted by a ring. Thin grey lines at low P and T indicate contours of constant opacity (Freedman et al. 2008), with $\log \kappa = -3.5$ to -1.0 (cm^2 g^{-1}) in steps of 0.5 dex, increasing with P.

To try to understand these luminosity scalings, we firstly note that the radiative luminosity at the radiative-convective boundary, which is equal to the total luminosity, can always be written as (Arras & Bildsten 2006)

$$L = \left(4\pi r^2 \frac{4acT^3}{3\kappa\rho} \frac{dT}{dr}\right)_{rcb} = \frac{16\pi Gac}{3} \frac{MT_{rcb}^4 \nabla_{adrcb}}{\kappa_{rcb} P_{rcb}}, \quad (2)$$

approximating the convection zone to contain the whole mass (cf. labels in Fig. 1) and radius. Thus, one way of obtaining $L(M, S)$ is to express the four quantities P_{rcb}, T_{rcb}, ∇_{adrcb} and κ_{rcb} in terms of M and S. This will now be done for the three regimes regimes in turn, starting with low entropies.

2.2.1 Low-entropy regime: $L \propto M^{0.7} f_{low}(S)$

To begin, consider the entropy dependence of luminosity at a fixed mass when $S \lesssim 9$–8 (at 1–10 M_J respectively). Fig. 1 reveals that the opacity at the radiative-convective boundary κ_{rcb} remains constant at a given mass, which provides a first relation. Secondly, over the temperature and pressure range of interest in this regime, the hydrogen and helium remain respectively molecular and neutral. This implies that ∇_{adrcb} is constant and that the entropy has a simple functional form in the ideal-gas approximation, given by the Sackur–Tetrode expression (e.g. Callen 1985). For an H$_2$–He I mixture with $Y = \frac{1}{4}$, this is

$$S = 9.6 + \frac{45}{32} \ln(T/1600\ K) - \frac{7}{16} \ln(P/3\ bar) \quad (3)$$

(hence $\nabla_{ad} = 0.31$), where $\ln 10 = 2.3$, and the reference T and P values were chosen for Section 2.2.2. Finally, T_{rcb} is approximately fit by $T_{rcb} \propto 10^{0.19S}$. Combining the four relations (constant ∇_{adrcb}
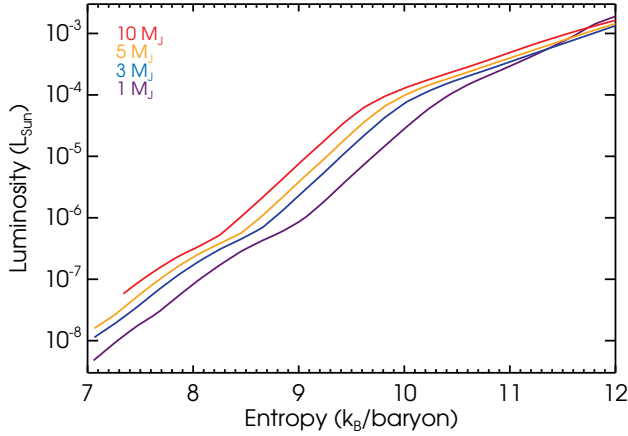
Figure 2. Luminosity as a function of entropy for our planet models. The masses shown are (bottom to top) $M = 1, 3, 5$, and 10 M_J. Here as throughout this paper, we use $L_{\rm Sun} = 3.86 \times 10^{33}$ erg s^{-1}.

and the three non-trivial ones) with equation (2) yields $L \propto 10^{1.04S}$. This is quite close to a power-law fit of Fig. 2, which gives $L \propto 10^{1.3S}$.

Next, consider the position of the RCB at fixed low entropy for different masses. Fixed entropy immediately implies $T \propto P^{\nabla_{\rm ad}}$, and the constant $\nabla_{\rm ad} = 0.31$ gives the second relation. The profiles of Fig. 1 indicate that in this low-entropy regime, the opacity depends approximately only on the pressure, with $\kappa \propto P^{0.9}$. Finally, we find that $P_{\rm rcb} \propto M^{0.5}$, thus providing the fourth relation. Combining these and using equation (2) gives $L \propto M^{0.8}$, in good agreement with a direct fit, which gives $L \propto M^{0.7}$.

Thus, a constant adiabatic gradient, an RCB opacity dependent only on the mass, and a few power laws suffice to show that in the low-entropy regime

$$L_{\rm low} = 10^{-7.7} L_\odot \left(\frac{M}{M_J} \right)^{0.7} 10^{1.3(S-7.5)}, \qquad (4)$$

which defines $f_{\rm low}(S)$ up to a constant. For Jupiter's adiabat with $T = 165$–170 K at 1 bar (Saumon & Guillot 2004) and thus an entropy of 6.71–6.75 k_B/baryon, this predicts $\simeq 1.9 \times 10^{-9}$ L$_\odot$, in good agreement with the current value L$_J = 8.7 \times 10^{-10}$ L$_\odot$.

2.2.2 *Intermediate-entropy regime: $L \propto M f_{\rm rz}(S)$*

We now look at intermediate entropies, which are in the range 9–10.2 (at 1 M_J) or 8.2–9.5 k_B/baryon (at 10 M_J). As explained by Arras & Bildsten (2006), equation (2) is of the form $L = M f(S)$, where $f(S)$ is a function of the entropy in the convection zone, only if the quantity $T^4 \nabla_{\rm ad}/\kappa P$ at the RCB is a function of a unique variable, S. The intermediate-S behaviour can then be understood by noticing in Fig. 1 that objects at those entropies have a $T_{\rm rcb}$ independent of internal entropy *and* an extended atmosphere (interrupted or not by a second convection zone). For these planets, the photosphere is sufficiently far from the RCB ($P_{\rm rcb} \gtrsim 10 P_{\rm phot}$, $T_{\rm rcb}^4 \gtrsim 5 T_{\rm eff}^4$) that the atmosphere merges onto the radiative-zero profile, which solves (Cox & Giuli 1968)

$$\frac{{\rm d}T}{{\rm d}P} = \frac{3}{16acG} \frac{L}{M} \frac{\kappa}{T^3}, \qquad (5)$$

where the boundary condition is by definition of no consequence. The solution is a $T(P)$ relation, which yields the radiative gradient $\nabla_{\rm rad} = {\rm d}\ln T/{\rm d}\ln P$ along it. The important point is that both

the atmosphere profile and its gradient depend only on the quantity L/M. Now, choosing an internal entropy fixes the adiabat, i.e. sets a second $T(P)$ relation. We require that at the intersection of the atmosphere and the adiabat $\nabla_{\rm rad}$ be equal to $\nabla_{\rm ad}$, which is the slope of the chosen adiabat. This thus pins down $\nabla_{\rm rad}$ in the atmosphere and hence L/M (and the atmosphere profile itself). Therefore, there is a unique L/M associated to an S, which means that L must be of the form[3] $L/M = f(S)$.

Since we use the Schwarzschild criterion $\nabla_{\rm ad} < \nabla_{\rm rad}$ to determine convective instability, where the radiative gradient is

$$\nabla_{\rm rad} = \frac{3LP}{16\pi acGMT^4} \kappa \qquad (6)$$

near the surface, and $\nabla_{\rm ad}$ is relatively constant, a slow inward increase of κ will ensure a deep RCB. Consequently, the $L \propto M f(S)$ scaling will hold for those M and S such that, starting at the photosphere with $P_{\rm phot} \simeq f(M)$ and $T_{\rm eff} \simeq f(P_{\rm phot}, S)$, the opacity increases only slowly along the adiabats. (For a power-law opacity $\kappa = \kappa_0 P^n T^{-n-s}$, this means $n/(n+s) \simeq \nabla_{\rm ad}$.) This is indeed the case for intermediate-S models in Fig. 1, where the $T(P)$ profiles are nearly aligned with contour lines of constant opacity. For this argument to hold, the radius must be rather independent of the mass (cf. Zapolsky & Salpeter 1969) and of the entropy. Also, one needs to approximate the entropy at the photosphere to be that of the interior, which is reasonable: even in the extended atmospheres, the entropy increases by at most $\simeq 0.5$ k_B/baryon.

The functional form of $f(S)$ can be obtained by fixing $T_{\rm rcb}$ and using equation (3) for the entropy of an ideal gas. The reference temperature of 1600 K was chosen based on the radiative-convective boundaries of Fig. 1. For convenience, $S(3 \text{ bar}, 1600 \text{ K})$ was computed using the interpolated SCvH tables. These include the contribution from the ideal entropy of mixing[4], a remarkably constant $S_{\rm mix} = 0.18$ k_B/baryon in a large region away from H$_2$ dissociation. Combining this $S(P, T)$ with equation (2), fixing $T = 1600$ K, and taking $\kappa(P, 1600 \text{ K}) \simeq 0.0104(P/3 \text{ bar})^{0.2}$ cm^2 g^{-1} from the interpolated table yields

$$\log_{10} \frac{L_{\rm rz}/L_\odot}{M/M_J} = -5.05 + 1.51(S - 9.6), \qquad (7)$$

i.e. $L = M f_{\rm rz}(S)$ with $f_{\rm rz}(S) = 3.4 \times 10^{28}$ erg s^{-1}M$_J^{-1}$ $10^{1.51(S-9.6)}$. (Thus, if $\kappa \propto P^n$ and ${\rm d}S/{\rm d}\ln P = -b$, $\log_{10} f_{\rm rz}(S) \propto (n+1)/b \ln 10$.) The subscript 'rz' highlights that the solution applies when the radiative zero solution is reached. This excellently fits the L/M–S relationship found in our grid of models at intermediate entropies.

2.2.3 *High-entropy regime: $L \propto M^{0.3} f_{\rm high}(S)$*

For $S \gtrsim 10$–9 (at 3–10 M_J, respectively), the luminosity becomes almost independent of mass at a given entropy. This indicates that the radiative solution does not hold anymore, and indeed Fig. 1 shows that planets with high entropy have atmospheres extending only over a small pressure range, with the more massive objects fully convective from the centre to the photosphere. The shortness of the atmosphere is due to the opacity's rapid increase inward, as constant-κ contours are almost perpendicular to $T(P)$ profiles in

---

[3] This regime was obtained by Arras & Bildsten (2006) when looking at irradiated planets. This can be roughly thought to fix $T_{\rm rcb}$ to the irradiation temperature, so that $T^4 \nabla_{\rm ad}/\kappa P$ at the RCB is automatically a function of only one thermodynamic variable, for instance S, for all entropies.

[4] We used the corrected version of the equations in SCvH; see the appendix of Saumon & Marley (2008).

that region. As in Section 2.2.1, we look at the behaviour of T, P, κ, and $\nabla_{\rm ad}$ at the RCB as a function of M and S.

Fig. 1 shows that at a fixed mass, $T_{\rm rcb}$ is almost indepedent of the (high) entropy, with the actual scaling closer to $T_{\rm rcb}{}^4 \propto 10^{0.2S}$. Also, $\kappa_{\rm rcb}$ is again mostly independent of S, as for the low entropies. At high entropies, $\nabla_{\rm adrcb}$ drops continuously with increasing S (decreasing $P_{\rm rcb}$), with a very rough $\nabla_{\rm ad} \propto 10^{-0.13S}$. For the fourth relation, we can fit $P_{\rm rcb} \propto 10^{-0.6S}$. Combining all this with equation (2) then gives $L \propto 10^{0.7S}$, which is quite close to a fit $L \propto 10^{0.6S}$.

At fixed high entropy, $\nabla_{\rm ad}$ is somewhat constant at 0.25–0.13 for $S = 10.5$–12. Also, above $\simeq 1500$ K and at $P < 1$ bar, the opacity is approximately independent of pressure, scaling only with temperature as $\kappa \sim T^4$. Finally, as in the low-entropy regime, $P_{\rm rcb} \propto M^{0.5}$; combining the four relations, we should have $L \propto M^a$ with $a \simeq 0.5$–0.4. This is not far from the direct fit $L \propto M^{0.3}$.

Therefore, the luminosity in the high-entropy regime is

$$L_{\rm high} = 10^{-3.88}\ {\rm L}_\odot \left(\frac{M}{{\rm M}_{\rm J}}\right)^{0.3} 10^{0.6(S-10.5)}, \tag{8}$$

which defines $f_{\rm high}(S)$ up to a multiplicative constant. Fig. 2 indicates that the coefficients are slightly different at the lowest masses ($M \lesssim 1.3\ {\rm M}_{\rm J}$ as it turns out), with the luminosity more sensitive on the mass, but this was ignored when obtaining equation (8).

Before summarising, let us briefly digress about the $P_{\rm rcb} \propto M^{0.5}$ scaling seen both at fixed low entropy and at fixed high entropy. In both cases, the model grid shows that, as a reasonable approximation, $P_{\rm rcb} \propto P_{\rm phot}$. At low entropies, R is constant, such that $P_{\rm rcb} \propto P_{\rm phot} = 2g/3\kappa \propto M/\kappa$. Then, the found $\kappa \sim P$ (see Section 2.2.1) immediately implies $P_{\rm rcb} \propto M^{0.5}$. At high entropies, planetary radii are significantly larger and vary, such that the radius dependence of the photospheric pressure should not be neglected; thus $P_{\rm phot} \propto M/R^2\kappa$. Fitting the $R(M, {\rm fixed\ high}\ S)$ relation in our models, we find $R \sim M^{-1.1}$ or $R \sim M^{-1.2}$, depending on the entropy. Then, $\nabla_{\rm ad} \simeq 0.2$ and $\kappa \sim T^4$ yield $\kappa \sim P^{0.8}$ at fixed S, and thus, isolating, $P_{\rm rcb} \sim M^{0.6}$ or $P_{\rm rcb} \sim M^{0.7}$. This is a slightly stronger dependence on mass than what is found in the grid, but the argument shows how the rough scaling can be derived.

2.2.4 Summary of luminosity scalings

In summary, we found from fitting the $L(M, S)$ relation across our planet models that $L \propto M^a 10^{\lambda S}$, with $a = (0.7, 1, 0.3)$ and $\lambda = (1.3, 1.5, 0.6)$ at low ($S \lesssim 9$–8, for 1–10 ${\rm M}_{\rm J}$ respectively), intermediate ($S \lesssim 10.2$–9.5) or high entropy, respectively. These scalings can be fit directly or more or less accurately derived by considering the behaviour of the different factors in equation (2).

Our approximate understanding of the different regimes is thus the following. For the conditions found in the atmospheres of intermediate-entropy planets, contours of constant opacity are almost parallel to adiabats. Since $\nabla_{\rm rad} \propto \kappa$ by equation 6 and, for a constant $\nabla_{\rm ad}$, only $\nabla_{\rm rad}$ determines when the atmosphere becomes convective, a slow inward increase of the opacity causes the radiative zone to extend over a large pressure range. This in turn means that the atmosphere can reach the radiative-zero solution, which we have shown necessarily implies $L = Mf(S)$. For the conditions found in the atmospheres of planets with high and low entropy, however, opacity increases relatively quickly along an adiabat. Since the $T(P)$ slope in the atmosphere is not too different from that of the convective zone's adiabat, this means that opacity increases rapidly in the atmosphere, which therefore cannot join onto the radiative-zero solution before becoming convective. The different $L(M, S)$ scalings then reflect in part the approximate

temperature- and pressure-*in*dependence of the opacity at low and high S, respectively. It is interesting to note that the transition from low to intermediate entropies is accompanied by a 'second-order' (i.e. relatively small) change in a and λ, while the the physical explanation changes to 'zeroth order'.

2.3 Cooling

With $L \propto M^a 10^{\lambda S}$, equation (1) implies $\mathrm{d}S/\mathrm{d}t = -M^{a-1}f(S)/\overline{T}$. Since hydrostatic balance yields $P_{\rm c} \sim GM^2/R^4$ and the convective core is adiabatic, we expect $\overline{T} \sim T_{\rm c} \propto (M^2/R^4)^{\nabla_{\rm ad}}$. (Across the whole grid, $\overline{T}/T_{\rm c} = 0.55$–0.63.) Therefore, at constant entropy and ignoring the radius dependence, $-\mathrm{d}S/\mathrm{d}t \propto M^{-2\nabla_{\rm ad}-1+a}$. This means that the entropy of a cooling planet should be approximately a function of $t/M^{2\nabla_{\rm ad}}$ when $a \simeq 1$ (at low and intermediate entropies), and that more massive planets cool more slowly (since a is always smaller than $2\nabla_{\rm ad} + 1 \simeq 5/3$). Thus, at fixed entropy, $L \propto M^a$, with $a = 0.3$–1, but at a fixed time the luminosity has a steeper dependence on M, closer to $L \propto M^2$, because more massive planets move to lower entropy more slowly. A more detailed analytic understanding of the cooling curves for irradiated planets along these lines was developed by Arras & Bildsten (2006).

2.4 Comparison with previous work

We now compare our cooling curves to classical hot starts. Fig. 3 shows cooling curves for large initial entropy compared to the hot-start models of Marley et al. (2007), the COND03 models (Baraffe et al. 2003) and those of Burrows et al. (1997), all of which use non-grey atmospheres with detailed opacities. The agreement is excellent, with our luminosities within the first 3 Gyr approximately within -30 and 20 per cent and -30 and 60 per cent above those of Baraffe et al. and Burrows et al.. (Of interest for the example of Section 4, our radii along the cooling sequence are at most approximately 0.08 and 0.04 ${\rm R}_{\rm J}$ (8 and 4 per cent) greater, respectively, as mentioned in Huang & Cumming (2012). This difference is comparable to the effect of neglecting heavy elements in the equation of state or not including a solid core (Saumon et al. 1996) and not significant for our purposes.) Our deuterium-burning phase at 20 ${\rm M}_{\rm J}$ ends slightly earlier than in Burrows et al. (1997) but this might be due to our simplified treatment of the screening factor.

Fig. 4 shows cooling curves for lower initial entropies than in Fig. 3. The cooling curves show the behaviour found by M07 and Spiegel & Burrows (2012) in which the luminosity initially varies very slowly, with the cooling time at the initial entropy much larger than the age of the planet. Eventually, the cooling curve joins the hot start cooling curve once the cooling time becomes comparable to the age.

Comparing to the cold starts in fig. 4 of M07, our models are a factor of $\simeq 3.5$–3.9 lower in luminosity for the same initial entropies, as given in their fig. 2. Increasing our initial entropies by 0.38 $k_{\rm B}$/baryon brings our cooling curves into agreement with theirs when the planet has not yet starting cooling. (For this comparison, we do not correct the time offset for the higher masses (see figs. 2 and 4 of M07), which are already on hot-start cooling curves at the earliest times shown.) Spiegel & Burrows (2012) computed the evolution of gas giants starting with a wide range of initial entropies. To compute the bolometric luminosity of their models, we take the published spectra and integrate the flux in the wavelength range given, 0.8–15 μm. The bottom panel of Fig. 4
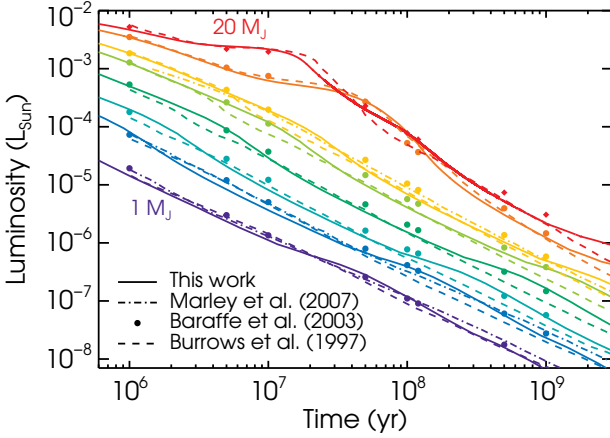
Figure 3. Cooling curves for (bottom to top) $M = 1, 2, 3, 5, 8, 10, 15,$ and $20\,M_J$ (solid curves) compared with the Marley et al. (2007) hot starts (for $M = 1, 2,$ and $10\,M_J$ only; dash-dotted curves), the COND03 tracks (dots) and the Burrows et al. (1997) models (dashed curves). The COND03 data is shown as dots because of insufficient sampling of the cooling tracks at higher masses.
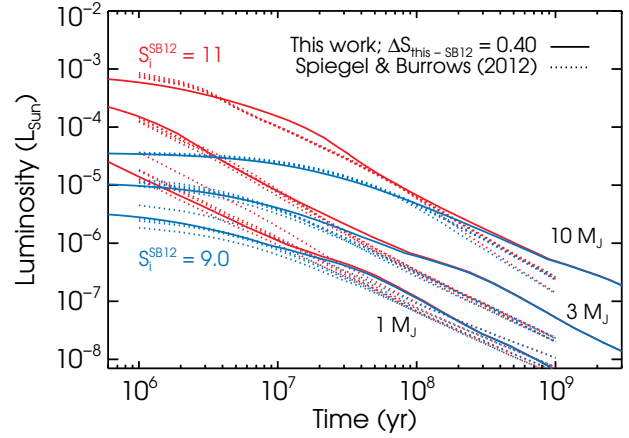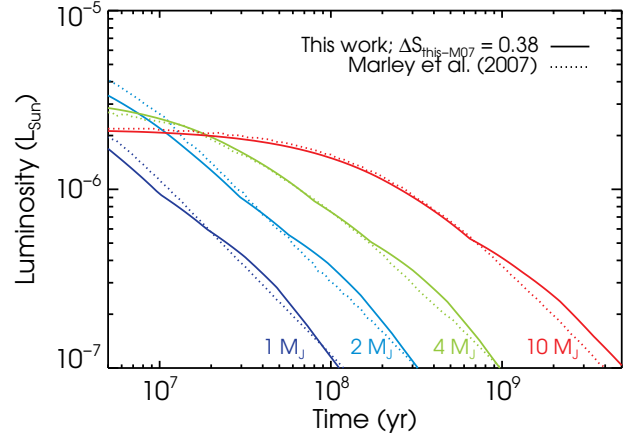

Figure 4. *Top panel:* Cooling curves for $M = 1, 2, 4, 10\,M_J$ and initial entropies equal to the Marley et al. (2007, M07) 'tuning-fork diagram' values $S_i = 9.23, 9.00, 8.60, 8.23$ (see their fig. 2) increased by 0.38. The dotted curves show the Marley et al. (2007) cooling tracks. *Bottom panel:* Cooling curves for $M = 1, 3, 10\,M_J$ (bottom to top) with initial entropies $S_i = 9.0$ and $S_i = 11$ increased by 0.40 (solid lines), compared to the models of Spiegel & Burrows (2012, SB12) with $S_i = 9.0$ and $S_i = 11$, to all four atmosphere types at each mass (dotted; hybrid-cloud or cloud-free, solar or three times solar metallicity). The truncation of the Spiegel & Burrows (2012) spectra causes an underestimate of the bolometric luminosity at late times (see text).

shows the comparison to all four models, with or without clouds and at solar or three times solar metallicity. Increasing our entropy by 0.40 k_B/baryon – e.g. comparing the Spiegel & Burrows (2012) model with $S = 9.0$ to ours with $S = 9.4$ – yields very good agreement, with our luminosities overlying their curves or within the spread due to the different atmospheres. The apparent disagreement at late times comes from the increasing fraction of the flux in the Rayleigh–Jeans tail of the spectrum beyond 15 μm. For comparison, the implied required bolometric correction is equal to 10 to 50 per cent of the flux in 0.8–15 μm for a blackbody with $T_{eff} \simeq 700$–300 K. From this and the hot-start T_{eff} tracks shown in Spiegel & Burrows (2012), we estimate that integrating the spectrum should give a reasonable estimate (to ca. 30 per cent) of the bolometric luminosity only up to $\simeq 50, 200,$ and 1000 Myr for objects with $M = 1, 3,$ and $10\,M_J$ respectively. This is indeed seen in Fig. 4.

In contrast with this is our nearly perfect agreement with the MESA stellar evolution code (Paxton et al. 2011, 2013). We compared our $L(S)$ relation to ones obtained from MESA at different masses (as in Fig. 2) and found that they are very nearly the same, with an entropy offset $\Delta S \lesssim 0.05$. We also produced grids with other opacities, using the MESA tables with the default $Y = 0.28$ and $Z = 0.02$, and the Freedman et al. (2008) tables with [M/H] = ±0.3 dex, and found that this changed the luminosity by at most $\simeq 10$ per cent. Similar differences were found to result from a changed helium mass fraction in the bulk of the planet. Therefore, it is not clear what might explain the small disagreement between the entropy values of these various authors. One possibility is a difference in the implementation of the SCvH equation of state, but this remains to be investigated.

The upshot of these comparisons to classical, non-grey-atmosphere hot and cold starts is that cooling tracks computed with the simple and numerically swift cooling approach described above can reproduce models which explicitly calculate the time dependence of the luminosity. When comparing models from different groups, one should keep in mind that there is a systematic uncertainty in the entropy values of $\Delta S_{syst} \simeq 0.4$. This is however small compared to the entropy difference between hot and cold starts.

3 GENERAL CONSTRAINTS FROM LUMINOSITY MEASUREMENTS

Masses of directly-detected exoplanets are usually inferred by fitting hot-start cooling curves (e.g. Burrows et al. 1997; Baraffe et al. 2003) to the measured luminosity of the planet, using the stellar age as the cooling time. Since the hot-start luminosity at a given age is a function only of planet mass, the measured luminosity determines the planet mass. Moreover, a planet's luminosity, at a given time and for a given mass, can never exceed that of the hot starts, since a larger initial entropy would have merely cooled onto the hot-start cooling track at an earlier age.

However, we have seen above that the luminosity at a given mass can be lowered by considering a sufficiently smaller initial entropy, which might be the outcome of more realistic formation scenarios (Marley et al. 2007; Spiegel & Burrows 2012). With the fact that luminosity increases with planet mass, this simple statement has important consequences for the interpretation of direct-detection measurements, namely that *there is not a unique mass*

which has a given luminosity at a given age. Cold-start solutions correspond to planets not having forgotten their initial conditions, specifically their initial entropy S_i, and every different initial entropy is associated to a different mass. In other words, a point in (t, L) space – a single brightness measurement – is mapped to a curve in (M, S_i) space. Since Marley et al. (2007) (but see also Baraffe et al. 2002; Fortney et al. 2005), it is generally recognised that direct detections should not be interpreted to yield a unique mass solution, but, with the exception of Bonnefoy et al. (2013), who used infrared photometry, this is the first time that this degeneracy is calculated explicitly.

3.1 Shape of the M–S_i constraints

The top panel of Fig. 5 shows the allowed masses and initial entropies for different values of luminosity $L_{bol}/L_\odot = 10^{-7}$, 10^{-6} and 10^{-5}, at ages of 10, 30, and 100 Myr. Below the deuterium-burning mass, constant-luminosity curves in the M–S_i plane have two regimes. At high initial entropies, the derived mass is the 'hot-start mass' independent of S_i since all S_i greater than a certain value have cooling times shorter than the age of the system. There, uncertainty in the stellar age translates directly into uncertainty in the planet mass: since $L \propto 1/t$ and $L \sim M^2$, the mass uncertainty is $\Delta M/M \simeq \frac{1}{2}\Delta t/t$. At lower entropies, the luminosity measurement occurs during the early, almost constant-luminosity evolution phase. Given a luminosity match in this region, one can obtain another by assuming a lower (higher) initial entropy and compensating by increasing (decreasing) the mass. As seen in Section 2, L is a very sensitive function of S at low and intermediate entropies, so that a small decrease in initial entropy must be compensated by a large increase in mass to yield the same luminosity at a given time; this yields the approximately flat portion of the curves. As long as the cooling time for a range of masses and entropies remains shorter than the age, *the entropy constraints do not significantly depend on the age.* The uncertainty in the initial entropy is $\Delta S_i \simeq 1/\lambda\,\Delta \log_{10} L_{bol}$, where $1/\lambda \simeq 0.7$ or 1.7 at low or high entropy (see Section 2.2.4). Finally, at higher masses, the possibility of an initial increase in the luminosity makes $L(t)$ non-monotonic and hence results in more complex geometries in the M–S_i plane. This will be discussed in a forthcoming publication.

The circles in the top panel of Fig. 5 show the initial entropies for cold- and hot-start models from M07, the 'tuning-fork diagram of exoplanets'. The entropies were increased by 0.38 k_B/baryon as in the top panel of Fig. 4 to match our models. Since the cooling time increases with mass (see Section 2.3), heavier planets of the hot-start (upper) branch, i.e. with arbitrarily high initial luminosity, have cooled less and are therefore at higher S. For their part, the cold-start entropies, which are still the post-formation ones, lie close to a curve of constant luminosity $L \simeq 2 \times 10^{-6}$ $L_\odot$. This reflects the fact that the post-formation luminosities in M07, as seen in their fig. 3, have similar values for all masses. The cause of this 'coincidence' is presently not clear; it might be a physical process or an artifact of the procedure used to form planets of different masses. Putting uncertainties in the precise values aside, the two prongs of the tuning fork in Fig. 5 give an approximate bracket within which just-formed planets might be found.

Mass information for a directly-detected planet can put useful constraints on its initial entropy and also potentially on its age and luminosity simultaneously. For instance, dynamical-stability analyses and radial-velocity observations (see Section 5) typically provide upper bounds on the masses. Since S_i decreases monotonically with M at a fixed luminosity, this translates into a *lower limit* on the
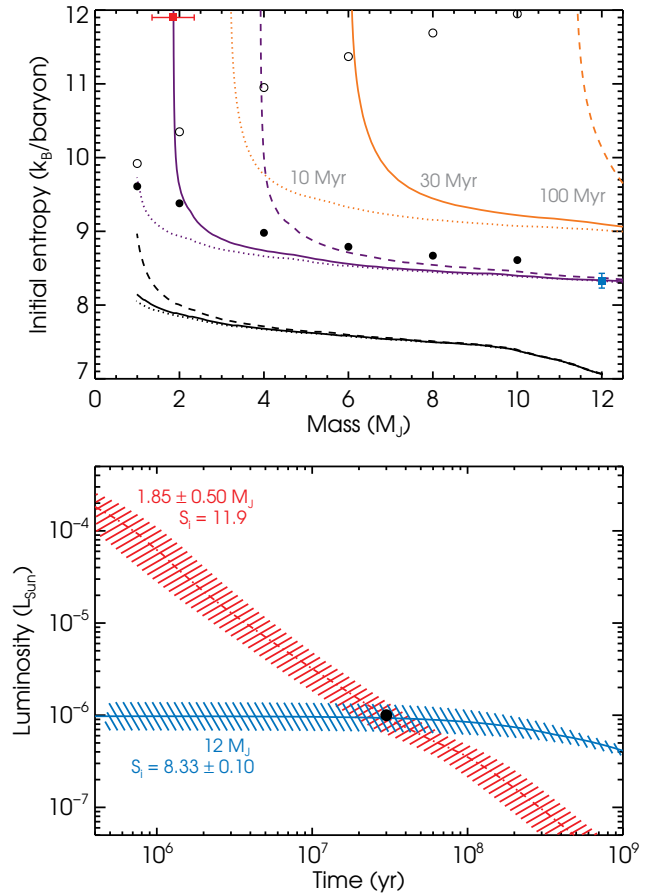

Figure 5. *Top panel:* Allowed values of planet mass M and initial entropy S_i corresponding to $L_{bol} = 10^{-7}$, 10^{-6}, and 10^{-5} $L_\odot$ (bottom to top sets of curves) and ages $t = 10$, 30, and 100 Myr (left to right or dotted, full and dashed lines). The circles show the results from Marley et al. (2007), increased by 0.38 k_B/baryon (cf. Fig. 4), for cold starts (filled circles) and hot starts (open circles), where the entropy is 1 Myr after the onset of cooling. Red and blue squares indicate the illustrative M and S_i used for the lightcurves in the bottom panel, with errorbars corresponding to the hatched regions there. *Bottom panel:* Two examples of cooling curves that have $L = 10^{-6}$ $L_\odot$ at 30 Myr. The dot-dashed (red) line has $M = 1.85$ M_J and $S_i = 11.9$ (hot start), while the full (blue) one has $M = 12$ M_J and $S_i = 8.33$ (cold start). Hashed regions indicate a spread of 0.5 M_J (0.1 k_B/baryon) for the hot- (cold-)start curve. The respective relative uncertainties are $\Delta M/M \simeq \frac{1}{2}\Delta t/t$ and $\Delta S_i \simeq 0.7\Delta \log_{10} L_{bol}$ for the cold- and hot-start cases, respectively (see text).

initial entropy. This has the potential of excluding the coldest-start formation scenarios. Conversely, a lower limit on the planet's mass implies an *upper* bound on S_i. If it is greater than the hot-start mass, this lower limit on the mass of a planet would be very powerful, due to the verticalness of the hot-star branch. Combined with the flatness of the 'cold branch' of the $M(S_i)$ curve, this could easily restrict the initial entropy to a dramatically small $\Delta S_i \simeq 0.5 \sim \Delta S_{syst}$. Also, the top panel of Fig. 5 shows that not all age and luminosity combinations are consistent with a given mass upper limit. Given the often important uncertainties in the age and the bolometric luminosity, this may represent valuable input.
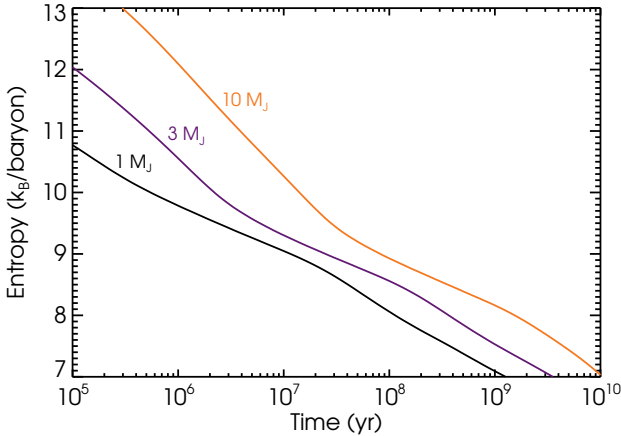
Figure 6. Entropy of hot starts as a function of time for planet masses of 1, 3, and 10 M_J (bottom to top). At a given age, the curve indicates the value of initial entropy above which the 'hot-start mass' applies. For a planet mass larger than the hot-start value, the initial entropy must be lower than the hot-start entropy at the current age.

3.2 Solutions on the hot- vs. cold-start branch

The bottom panel of Fig. 5 shows lightcurves illustrating the two regimes of the $M(S_i)$ curves discussed above. The hot-start mass is 1.85 M_J, whereas the selected cold-start case ($S_i = 8.33$) has $M = 12 \, M_J$ – i.e. *a six times larger mass* – and both reach $\log L_{bol}/L_\odot = -6$ at $t = 30$ Myr, with the cold-start values essentially independent of age. The hatched region around the 1.85-M_J curve comes from hot-start solutions between 1.35 and 2.35 M_J and is within a factor of two of the target luminosity, showing the moderate sensitivity of the cooling curves to the mass. However, in the cold-start phase, a variation by a factor of two can also be obtained by varying at a fixed mass the initial entropy from 8.23 to 8.43 k_B/baryon. This great sensitivity implies that combining a luminosity measurement with information on the mass would yield, if some of the hot-start masses can be excluded, tight constraints on the initial entropy.

3.3 Definition of 'hot-start mass'

By showing the entropy of hot starts as a function of time, Fig. 6 provides another way of looking at Fig. 5. Given a mass obtained from hot-start cooling tracks, the entropy value at that time read off from the curves indicates what 'hot' is, i.e. provides a lower bound on the initial entropy if the hot-start mass is the true mass. If however the planet is more massive, this entropy value is instead an upper bound on the post-formation entropy.

Since it has no bearing upon the detections considered below, we defer a similar discussion concerning deuterium-burning objects to a later work. As noted before, the possibility of an initial increase in the luminosity with time can complicate the form of the $M(S_i)$ constraints.

4 GENERAL CONSTRAINTS FROM GRAVITY AND EFFECTIVE-TEMPERATURE MEASUREMENTS

Before applying the analysis described in the previous section to observed systems, it is worth discussing a second way by which constraints on the mass and initial entropy can be obtained. The idea is to firstly derive an object's effective temperature and surface gravity by fitting its photometry and spectra with atmosphere models. Integrating the best-fitting model spectrum gives the luminosity, and this can be combined with T_{eff} and $\log g$ to yield the radius and the mass. This procedure was described and carefully applied by Mohanty et al. (2004) and Mohanty, Jayawardhana, & Basri (2004). However, one can go further: considering models coupling detailed atmospheres with interiors at an arbitrary entropy, the mass and radius translate into a mass and current entropy. Then, using cooling tracks beginning with a range of initial conditions, the initial state of the object can be deduced given the age. Thus, in contrast to the case when only luminosity is used, M and S_i can both be determined without any degeneracy between the two.

In practice, however, there seems to be too much uncertainty in atmosphere models for this method to be currently reliable, as the work of Mohanty et al. shows. Their sample comprised a dozen young (~ 5 Myr) objects with $T_{eff} \simeq 2600$–2900 K[5] with high-resolution optical spectra. The combined presence of a gravity-sensitive Na I doublet and effective-temperature-sensitive TiO band near 0.8 μm allowed a relatively precise determination of $\log g$ and T_{eff} for most objects, with uncertainties of 0.25 dex and 150 K (Mohanty et al. 2004). However, there were significant offsets in the gravity ($\simeq 0.5$ dex) of the two coldest objects with respect to model predictions of Baraffe et al. (1998) and Chabrier et al. (2000). Mohanty et al. (2004) came to the conclusion that the models' treatment of deuterium burning, convection[6] or accretion – i.e. the assumed initial conditions – are most likely responsible for this disagreement at lower T_{eff}. Moreover, the more recent work of Barman et al. (2011b) (see Section A1.1 below) indicates that 'unexpected' cloud thickness and non-equilibrium chemistry may compromise a straightforward intepretations of spectra in terms of gravity and temperature for young, low-mass objects. Nevertheless, with the hope that future observations will allow a reliable calibration of atmosphere models, we illustrate with an example how M and S_i can be determined for an object from its measured T_{eff} and $\log g$.

Fig. 7 shows the constraints on the current mass and entropy of a planet with $\log g = 4.00 \pm 0.25$ (cm s^{-2}) and $T_{eff} = 900 \pm 50$ K, where the uncertainties in the gravity and effective temperature are the possible accuracy reported by Mohanty et al. (2004) and thus correspond to an optimistic scenario. The constraints are obtained by simultaneously solving for M, S, R, and L given T_{eff} and $\log g$, with the $L(M, S)$ and $R(M, S)$ relations given by our model grid. The required mass and current entropy are $M = 6.5 \, M_J$ and $S = 9.2$, with the 1-σ ellipse between 4.0–10.1 M_J and 9.0–9.3 k_B/baryon. The large uncertainty in the mass (the width of the ellipse) is dominated by the uncertainty in the gravity, since radius is roughly constant at these entropies. We note that non-Gaußian errorbars are trivial to propagate when determining mass and entropy in this way since it is only a matter of mapping each ($\log g$, T_{eff}) pair to an (M, S) point.

Since this M–S determination concerns only the current state, it is independent of the cooling sequence, in particular of the 'hot vs. cold start' issue. Nevertheless, with this approach, it is immedi-

---

[5] The spectral types are $\simeq$ M–M7.5, but Mohanty, Jayawardhana, & Basri (2004) stress that the correspondence between spectral type and effective temperature of young objects has not yet been empirically established and thus that calibration work (in continuation of theirs) remains to be done.

[6] Qualitatively, their finding that theoretical tracks predict too quick cooling at low masses might be evidence for the argument of Leconte & Chabrier (2012) that convection in the interior of these objects could be less efficient than usually assumed.
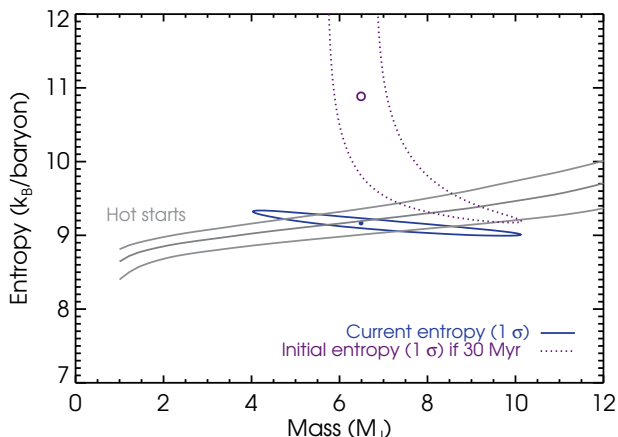
Figure 7. Constraints on the mass and entropy of an example planet from its gravity and effective temperature, with $\log g = 4.00 \pm 0.25$ (cm s^{-2}) and $T_{\text{eff}} = 900 \pm 50$ K (and thus optimistic errorbars; see text). The mass and current entropy corresponding to $\log g = 4.00$ and $T_{\text{eff}} = 900$ K are shown by a filled circle. The narrow ellipse (solid line) is the 1-σ confidence region in the mass and *current* entropy, whereas the deformed ellipse (dotted line) shows the constraints on the *initial* entropy assuming an age of 30 Myr. The open circle corresponds to the 'measured' central value. The three solid grey lines indicate the entropy of hot starts at 20, 30, and 50 Myr (top to bottom). Higher masses can be seen to cool more slowly (see Section 2.3).

5 COMPARISON WITH OBSERVED OBJECTS

5.1 Directly-detected objects

Neuhäuser & Schmidt (2012) recently compiled and homogenously analysed photometric and spectral data for directly-imaged objects and candidates, selecting only those for which a mass below 25 M$_J$ is possible[7]. They report for each of the 28 objects a luminosity and effective temperature, which they either take from the original papers or calculate, usually from bolometric corrections when a spectral type or colour index is available or brightness difference with the primary when not. Neuhäuser & Schmidt then use a number of hot-start cooling models to derive (hot-start) mass values along with errorbars, while recognising that hot starts suffer from uncertainties at early ages.

In this Section, we determine joint constraints on the masses and initial entropies of directly-detected objects, focussing on the ones for which (tentative) additional mass information is available. This is then a generalisation, for the objects we consider, of the analysis of Neuhäuser & Schmidt (2012). A proper statistical analysis of the set of $M(S_i)$ curves would be challenging at this point due to the inhomogeneity of the observational campaign designs. However, upcoming surveys should produce sets of observations with well-understood and homogenous biases, convenient for a statistical treatment.

Before turning to specific objects, we display in Fig. 8 the data[8] collected and computed by Neuhäuser & Schmidt (2012) along with hot- and cold-start cooling tracks for different masses. This is an update of the analogous figures of Marley et al. (2007, M07) and Janson et al. (2011), which had only a handful of data points. This shows that there are already many data points which – at least based solely on their luminosity – could be explained by cold, warm, or hot starts, highlighting the importance of being open-minded about the initial entropy when interpreting these observations.

There are two features of the data distribution in Fig. 8 which immediately stand out. The first is that the faintest young objects are brighter than the faintest oldest objects, i.e. that the minimum detected luminosity decreases with the age of the object. Moreover, this minimum, with the exception of data points (7) and (28), approximately follows the cooling track of hot-start objects of $\simeq 7$ M$_J$. The second feature is the absence of detections between the hot-start 10- and 15-M$_J$ cooling curves, roughly between 20 and 100 Myr. More accurately, there is, in a given age bin in that range, a lower density of data points with luminosities around 10^{-4} L$_\odot$ than at higher or lower luminosities.

A proper assesment of the statistical significance of this 'gap' in the data points would require taking both the smallness of the number of detections around 40 Myr and the biases and non-detections of the various surveys into account. However, it would not be surprising if the underdensity in the luminosity function dN/dL of the data points, at a fixed age, proved to be real, since there is also a suggestive underdensity in the cooling curves. Indeed, the onset of deuterium burning near 13.6 M$_J$ slows down the cooling, which breaks the hot-start scaling $L \propto t^{-1}$ (see Section 2.3)

ately apparent what constraints the age imposes on the initial conditions. Indeed, not all (M, S) are consistent with an age since no planet of a given mass can be at a higher entropy than the hot-start model at that time (see Fig. 6. The entropy of hot starts is shown in Fig. 7 after 10, 30, and 50 Myr. The 30-Myr age excludes objects with $M \lesssim 6$ M$_J$, which is the hot-start mass of this example. Considering only hot-start evolution sequences would have been equivalent to requiring the solution to be on one of the hot-start (grey) curves. This is however a restriction which currently could not be justified, given our ignorance about the outcome of the formation processes.

The dotted lines in Fig. 7 indicate the derived constraints on the initial entropy, assuming an age of 30 Myr. These constraints are similar to ones based on luminosity (see Fig. 5) but are somewhat tighter since an upper mass limit is provided by the measurement of $\log g$. Even within a set of models, i.e. putting aside possible systematic issues with the atmospheres of young objects, it is however often the case that the surface gravity is rather ill determined (as for the objects discussed below in Section 5). In this case, provided a sufficiently large portion of the spectrum is covered, we expect the approach based on the bolometric luminosity presented in this work to be more robust than the derivation of constraints from effectively only the surface temperature. Indeed, the former avoids compounding uncertainties in T_{eff} with those in the radius in an evolutionary sequence, which can be further affected by the presence of a core (of unknown mass). With both sustained modelling efforts and the detailed characterisation of an increasing number of detections, one may hope that reliable atmosphere models for young objects will become available in a near future, allowing accurate determinations of the mass, radius, and initial entropy of directly-detected exoplanets.

---

[7] This value was chosen by Schneider et al. (2011) as an approximation to the 'brown-dwarf desert', which is a gap in the mass spectrum between $\simeq$ 25–90 M$_J$ (Marcy & Butler 2000; Grether & Lineweaver 2006; Luhman et al. 2007; Dieterich et al. 2012).

[8] Despite doubts about its nature or existence (e.g. Janson et al. 2012; Currie et al. 2012a), we leave the reported values for Fomalhaut b in this plot and also show the revised age of Mamajek (2012).
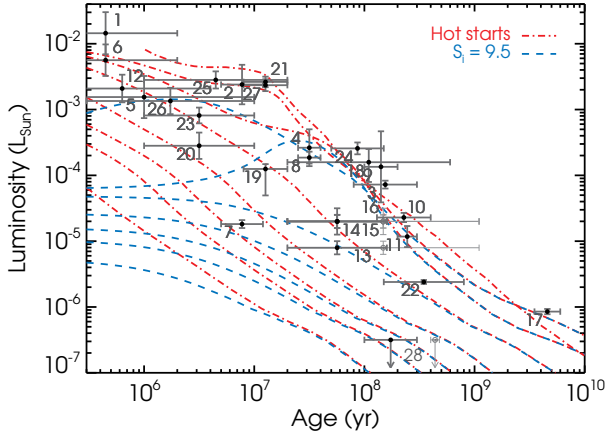
Figure 8. Directly-observed objects with a hot-start mass < 25 M_J (Neuhäuser & Schmidt 2012) compared with cooling curves for M = 1, 2, 3, 5, 10, 15, 20, and 25 M_J (bottom to top), for S_i = 9.5 (dashed) and hot starts (dash-dotted); the 25-M_J curve is from Burrows et al. (1997) and has no cold-start equivalent. Since their uncertainties are large, the central age values are taken as the geometric mean of the upper and lower bounds reported (only RXJ1609 B/b, GSC 8047 B/b, and HIP 78530 B/b have a reported best age, for all three of 5 Myr). The errorbars for the HR 8799 planets go up to 160 Myr and do not include the Moya et al. (2010b) astero-seismology measurement of 1.1–1.6 Gyr since it is not used in our analysis (see Section A2.1). However, wider paler errorbars with a ring symbol do use the upper value of 1.1 Gyr (as reported by Neuhäuser & Schmidt 2012). Note that data points (14) and (15) overlap, differing only in their verti-cal errorbars. The upper limit for Fomalhaut b is included, also with the revised, greater age from Mamajek (2012) as a paler ring symbol, despite uncertainties about is existence. The data points are, with in boldface those investigated more closely below: (1) GG Tau Bb, (2) TWA 5 B, (3) GJ 417 BC, (4) GSC 8047 B/b, (5) DH Tau B/b, (6) GQ Lup b, **(7) 2M1207 b**, (8) AB Pic B/b, (9) LP 261-75 B/b, (10) HD 203030 B/b, (11) HN Peg B/b, (12) CT Cha b, (**13, 14, 15, 16**) **HR 8799 bcde**, (17) Wolf 940 B/b, (18) G 196-3 B/b, (**19**) *β* **Pic b**, (20) RXJ1609 B/b, (21) PZ Tel B/b, (22) Ross 458 C, (23) GSC 6214 B/b, (24) CD-35 2722 B/b, (25) HIP 78530 B/b, (26) SR 12 C, (27) HR 7329 B/b, (28) Fomalhaut b.

and leads to a greater distance between the hot-start cooling curves for 10 and 15 M_J than for 5 and 10 M_J. (This is clearly visible in fig. 1 of Burrows et al. (2001), which also shows that there is a similar gap for low-mass stars at 10^{-4} $L_\odot$ and 1–10 Gyr, due to the hydrogen main sequence.) In particular, cooling tracks for objects of 15, 20, and 25 M_J nearly overlap at ∼ 100 Myr around 10^{-4} $L_\odot$, where data points and their errorbars collect too. This tentative in-dication of an agreement between the detections and the cooling tracks suggests that the latter might be consistent with the data[9]. It will therefore be interesting to see how significant the gap is and how it evolves as data points are added to this diagram.

We finally note that, in Fig. 8, the best-fitting age is cal-culated as the geometric mean of the reported upper and lower

---

[9] Cold-start curves too show this gap, to the extent that the luminosity rise due to deuterium burning is very sensitive to the initial entropy (see Fig. 8), which would need to be set accordingly finely to have the lightcurves pass through the data gap. The implicit assumptions here are that the observed distribution of masses is uniform in the approximate range 5–25 M_J (as are the mass values chosen for Fig. 8), and that the same applies to the initial entropy. The former cannot currently be validated but the latter seems reasonable, as the entropy interval over which cooling curves change from going above to below the gap is very narrow.

bounds since, in most cases, no best-fitting value is provided, and the bounds are typically estimates from different methods, which cannot be easily combined. In fact, the ages of young ($\lesssim$ 500 Myr) stars are in general a challenge to determine, as Soderblom (2010) reviews, and represent the main uncertainty in direct observations. Moreover, as Fortney et al. (2005) point out, assuming co-evality of the companion and its primary may be problematic for the youngest objects. Indeed, a formation timescale of $\simeq$ 1–10 Myr in the core-accretion scenario would mean that some data points of Fig. 8 be-low ∼ 10 Myr may need to be shifted to lower ages, by an un-known amount. This consideration is thus particularly relevant for GG Tau Bb, DH Tau B/b, GQ Lup b, and CT Cha b (data points 1, 5, 6, and 12), which are all possibly younger than 1 Myr, and would require a closer investigation.

We now provide detailed constraints for three planetary systems, chosen for the low hot-start mass of the companion (2M1207 b) or because additional mass information is available (HR 8799 and β Pic).

5.2 2M1207

The companion to the brown dwarf 2MASSWJ 1207334–393254 (2M1207 A, also known as TWA 27 A; Gizis 2002) is the first directly-imaged object with a hot-start planetary mass (Chauvin et al. 2004, 2005). Since the age and luminosity of 2M107 b are the inputs for our analysis, they are discussed in some detail in Section A1, along with tentative information on the mass. We adopt an age of 8^{+4}_{-3} Myr (Chauvin et al. 2004; Song et al. 2006) and a luminosity of log $L/L_\odot$ = -4.68 ± 0.05 (Barman et al. 2011b), and assume that deuterium-burning masses above $\simeq$ 13 M_J (Spiegel, Burrows, & Milsom 2011) are excluded.

Fig. 9 shows the joint constraints on the mass and initial en-tropy of 2M1207 b based on its luminosity and age. We recover the hot-start mass of 3–5 M_J (Barman et al. 2011b) but also find solutions at higher masses. If deuterium-burning masses can be excluded, the formation of 2M1207 b must have led to an initial entropy of $S_i \geqslant$ 9.2, with an approximate formal uncertainty on this lower bound of 0.04 k_B/baryon (see Section 3.1) due solely to the luminosity's statistical error, independent of the age's. This initial entropy implies that the M07 cold starts are too cold by 0.7 k_B/baryon, roughly independently of the mass, to explain the formation of this planet. This is consistent with the timescale-based conclusion of Lodato, Delgado-Donate, & Clarke (2005) that core accretion cannot be responsible for the formation of this system *if* one also accepts the received wisdom that core accretion neces-sarily leads to the coldest starts. However, our robust quantitative finding is more general, in that it provide constraints on the result of the formation process which are *model-independent*.

To show how these $M(S_i)$ constraints can easily be made even more quantitative and thus suitable for statistical analyses, we ran a Metropolis–Hastings Markov-Chain Monte Carlo (MCMC; e.g. Gregory 2005) in mass and entropy with constant priors on these quantities. Uncertainties in the luminosity L and age t were in-cluded in the calculation of the χ^2 by randomly choosing an 'ob-served' L_{obs} and a stopping time for the cooling curve t_{stop} at every step in the chain. The quantity log L_{obs} was drawn from a Gaußian defined by the reported best value and its errorbars, and t_{stop} from a distribution which is either constant in t between the adopted up-per and lower limits t_1 = 5 Myr and t_2 = 12 Myr and zero oth-erwise, or lognormal in t, centered at $t_0 = \sqrt{t_1 t_2}$ = 7.7 Myr and with $\sigma_{\log t}$ = log t_2/t_1 = 0.19 dex. The results are shown along the vertical axis of Fig. 9 for four different assumptions. To obtain the
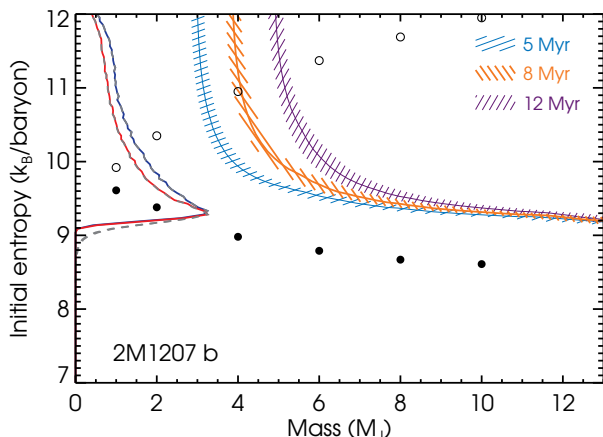
Figure 9. Allowed values of planet mass M and initial entropy S_i for 2M1207 b for assumed ages of 8^{+4}_{-3} Myr. The luminosity is that of Barman et al. (2011b), $\log L_{bol}/L_\odot = -4.68 \pm 0.05$, with the hatched regions corresponding to curves within $\pm 1\,\sigma$ of the luminosity values and the thick lines to the central value. The curves along the vertical axis show posterior distributions from MCMCs with different mass priors and assumed luminosity distributions. The solid curves only have an upper mass limit of 13 M_J, while the dashed curves include solutions in the deuterium-burning region, up to 20 M_J. For the blue curve (further from the left axis) and the corresponding dashed grey posterior (practically identical), a log-normal error distribution in time centered at $\sqrt{5 \times 12} \simeq 7.7$ Myr and of width 0.19 dex was used, while the red curve and corresponding dashed line are for a flat distribution in time between 5 and 12 Myr (and zero otherwise). The circles show the results from Marley et al. (2007), increased by 0.38 k_B/baryon (cf. Fig. 4), for cold starts (filled circles) and hot starts (open circles), where the entropy is 1 Myr after the onset of cooling.

two solid lines, we applied an upper mass cut at 13 M_J and took a lognormal (less peaked curve) or a top-hat (more peaked) distribution in time. The dashed curves come from the same MCMC chains but with a mass cut-off of 20 M_J, i.e. including deuterium-burning objects. Because of the delayed cooling due to deuterium burning, the required initial entropy drops down faster with mass than in the cold-start branch, such that lower S_i values are possible. At 20 M_J, the required S_i is 8.2, but it is still only 9 k_B/baryon at 15 M_J. However, the phase space for high masses is very small since the initial entropy needs to be extremely finely tuned; hence the smallness of the effect on the posteriors. As Fig. 9 shows, different assumptions on the luminosity, age, and mass priors all lead to similar results for the initial entropy, namely that $S_i \gtrsim 9.2$ and that there are more solutions near this lower limit.

5.3   HR 8799

We now turn to the only directly-imaged system with multiple objects for which planetary masses are possible, HR 8799. The age of the system and the luminosities of the companions are discussed in Section A2, along with information on the mass. We consider ages of 20 to 160 Myr, close to the values of Marois et al. (2008), and use the standard luminosities of $\log L_{bol}/L_\odot = -5.1 \pm 0.1$ (HR 8799 b), -4.7 ± 0.1 (cd) and -4.7 ± 0.2 (e) from Marois et al. (2008, 2010). It also seems resonable to assume that deuterium-burning masses can be excluded for all objects, thanks to the (preliminary) results from simulations of the system's dynamical stability.

Fig. 10 shows the joint constraints on the masses and initial entropies of HR 8799 b, d, and e. Uncertainties in the age are
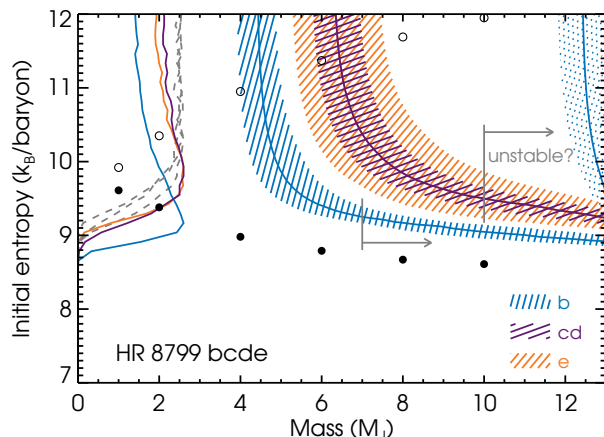

Figure 10. Allowed values of planet mass M and initial entropy S_i for HR 8799 b ($\log L_{bol}/L_\odot = -5.1 \pm 0.1$; blue bands), HR 8799 cd (-4.7 ± 0.1; purple), and HR 8799e (-4.7 ± 0.2; orange) for assumed ages of 20 (lower-mass group) and 160 Myr (higher-mass band; planets cde are outside the plotting range). Luminosities are from Marois et al. (2008, 2010), and nearly in agreement with Marley et al. (2012). The lines correspond to the best-fitting luminosity values, while the hatched regions use the 1-σ error-bars. Along the left axis are shown the posterior distributions in S_i (colours as for the M–S_i hashed bands), with no particular relative normalisation. These were obtained from an MCMC, taking luminosity and age uncertainties into account based on lognormal distributions (see text), and using flat priors in S_i and M. The mass upper cut-off is $M_{max} = 13$ M_J (full lines) or $M_{max} = (7, 10, 10, 10)$ M_J (for planets bcde, respectively; dashed lines), since analyses of the system's dynamical stability seem to indicate that higher masses are unstable. This is indicated by the vertical line segments with arrows in the direction of the excluded masses. The circles show the results from M07, increased by 0.38 k_B/baryon (cf. Fig. 4), for cold starts (filled circles) and hot starts (open circles), where the entropy is 1 Myr after the onset of cooling.

taken into account by considering the two extremes of 20 Myr and 160 Myr separately, while the 1-σ errors in the luminosities are reflected by the width of the hatched regions. We find hot-start masses for 20 Myr of $4.4^{+0.4}_{-0.5}$ (b), 6.3 ± 0.6 (cd), and 6 ± 1 M_J (e), where the errorbars here come only from those on the luminosity. These values are in good agreement with Neuhäuser & Schmidt (2012) and are similar to the usually-cited 30-Myr values of $(5, 7, 7, 7)$ M_J (Marois et al. 2010). The hot-start masses for 160 Myr are above 12 (HR 8799 b) and 13 M_J (cde), and the $M(S_i)$ constraints for the latter three are not shown since they are within the deuterium-burning regime.

Excluding deuterium-burning masses for all objects and using only the luminosity measurements, Fig. 10 shows that all planets of the HR 8799 system must have formed with an initial entropy greater than 9 k_B/baryon, with $S_i \gtrsim 8.9$ for b, $S_i \gtrsim 9.2$ for c and d, and $S_i \gtrsim 9.1$ for e. (When comparing models of different groups, one should remember that there is typically a systematic uncertainty in entropy values of $\Delta S_{syst} \simeq 0.4$, as mentioned in Section 2.4.) Using tentative upper mass limits of 7 and 10 M_J, respectively, the lower bounds on the initial entropies can be raised to 9.2 (b) and 9.3 k_B/baryon (cde) if one takes the conservative scenario of the 1-σ lower luminosities value at 20 Myr. These lower bounds on the entropy are however mostly independent of the age because they are set by cold-start solutions, where the age is much smaller than the cooling time at that entropy. Formal uncertainties on the lower bounds due to those in the luminosities are (see Section 3.1) approximately 0.07 (bcd) or 0.14 k_B/baryon (e) and thus negligible.

Here too we ran an MCMC to derive quantitative constraints on the initial entropy of each planet. The quantity $\log L_{\mathrm{obs}}$ was drawn from a Gaußian defined by the reported best value and its errorbars, and t_{stop} from a distribution which is either constant in t between the adopted upper and lower limits $t_1 = 20$ Myr and $t_2 = 160$ Myr and zero otherwise, or lognormal in t, centered at $t_0 = \sqrt{t_1 t_2} = 57$ Myr and with $\sigma_{\log t} = \log t_2/t_1 = 0.9$ dex. Posteriors on the initial entropy for each of the HR 8799 planets are shown along the vertical axis in Fig. 10, using a flat prior in S_{i} and a mass prior constant up to an M_{max} and zero afterward. The cases 'without mass constraints' ($M_{\mathrm{max}} = 13$ M_{J}) are nearly constant in S_{i}, especially for planet b, but show a peak near cold-branch values of 9 and 9.5 k_{B}/baryon for HR 8799 b and cde. Adding mass information from dynamical-stability simulations by taking $M_{\mathrm{max}} = (7, 10, 10, 10)$ M_{J} flattens the S_{i} posterior and shifts the minimum bounds at half-maximum from $(8.9, 9.2, 9.2, 9.2)$ to $(9.3, 9.5, 9.5, 9.4)$ k_{B}/baryon, respectively. We note that these results are insensitive to both the form of the uncertainty in t and the use of a non-flat prior in mass (as shown below for β Pic in Section 5.4).

Comparing to the 'tuning fork' entropy values reproduced in Fig. 10, we find that the coldest-start models of M07 cannot explain the luminosity measurements for the HR 8799 planets. Spiegel & Burrows (2012) and Marley et al. (2012) also came to this conclusion, with the latter noting that 'warm starts' match the luminosity constraints. It is now possible to say specifically that *the Marley et al. (2007) cold starts would need to be made $\Delta S \simeq 0.5$ k_{B}/baryon hotter to explain the formation of the HR 8799 planets*. Given that the precise outcomes of the core accretion and gravitational instability scenarios are uncertain and that this system represents a challenge for both (as Marois et al. 2010 and Currie et al. 2011 review), quantitative comparisons such as our procedure allows should be welcome to help evaluate the plausibility of the one or the other.

We note in passing that one needs to take care also when interpreting the measurements of Hinkley et al. (2011a) and Close & Males (2010). These authors measured upper limits on the brightness of companions within 10 AU and between 200 and 600 AU from the star, respectively. However, both groups then used the hot-start models of Baraffe et al. (2003) to translate the brightness limits into masses (11 M_{J} at 3–10 AU and 3 M_{J} within 600 AU). Therefore, since colder-start companions would need to be more massive to have the same luminosity, what they provide are really *lower* upper limits on the mass of possible companions. How much higher the masses could realistically be in this case is hard to estimate without a bolometric luminosity, but there is an important general point: without the restriction of considering only hot-start evolutionary tracks, *luminosity upper limits do not provide unambiguous mass constraints*. Incidentally, this more general view of the results of Hinkley et al. (2011a) means that the unseen companion evoked by Su et al. (2009) as the possible cause of the inner hole (at $\lesssim 6$ AU) does not have to be of small mass. This inner object would nevertheless have to be consistent with the results of dynamical stability simulations.

5.4 β Pic

A companion to the well-studied star β Pic was first observed in 2009 (Lagrange et al. 2009; Bonnefoy et al. 2011) and, very recently, it became the first directly-detected object with a planetary mass for which radial-velocity data is also available. The age of the system is 12^{+8}_{-4} Myr (Zuckerman et al. 2001), and we discuss in
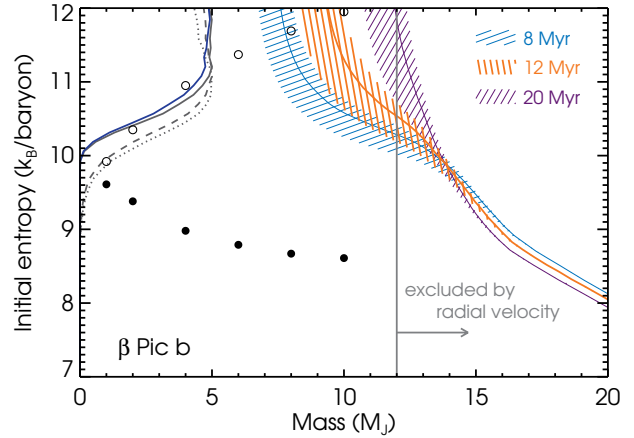

Figure 11. Allowed values of planet mass M and initial entropy S_{i} for β Pic b using our estimated $\log L_{\mathrm{bol}}/L_{\odot} = -3.90^{+0.05}_{-0.12}$ and an age of 12^{+8}_{-4} Myr. The hatched regions correspond to luminosity values within the (asymmetrical) 1-σ interval, with the central values marked by thick lines. The curves along the vertical show the marginalised posterior distribution on S_{i} from an MCMC simulation using the luminosity and age values and their uncertainties. These were taken to be lognormal but asymmetric for the luminosity, and lognormal in time, centered at $t_0 = \sqrt{8 \times 20} = 12.7$ Myr with a standard deviation of 0.35 dex. The full blue line (closer to the vertical axis) results from the (M, S_{i}) distribution being multiplied by a $\mathrm{d}N/\mathrm{d}M \propto M^{\alpha}$ prior, with $\alpha = -1.3$ (Cumming et al. 2008; Nielsen & Close 2010), and zero for $M > 12$ M_{J}, while the full grey posterior has only a mass cut at 12 M_{J}, from the Lagrange et al. (2012b) radial-velocity constraint. The dashed and dotted curves both have an upper mass cut of 20 M_{J}, with and without the $\mathrm{d}N/\mathrm{d}M$ prior applied, respectively. The circles show the results from Marley et al. (2007), increased by 0.38 k_{B}/baryon (cf. Fig. 4), for cold starts (filled circles) and hot starts (open circles), where the entropy is 1 Myr after the onset of cooling.

detail in Section A3 how we derive a bolometric luminosity[10] of $\log L_{\mathrm{bol}}/L_{\odot} = -3.90^{+0.05}_{-0.12}$.

Fig. 11 shows the $M(S_{\mathrm{i}})$ constraints available for β Pic b from our luminosity estimate and the radial-velocity (RV) constraint. We recover a hot-start mass $\simeq 9.5 \pm 2.5$ M_{J}, in agreement with Quanz et al. (2010) and Neuhäuser & Schmidt (2012), but additionally find that higher masses are consistent with the luminosity measurement. Excluding solutions where deuterium burning plays an important role in the evolution of the object (recognisable by the extreme thinness of the constant-luminosity $M(S_{\mathrm{i}})$ curve) implies that $S_{\mathrm{i}} \geqslant 9.8$. Using the RV mass upper limit, these constraints on the initial entropy can be made tighter: with an age of 12 Myr, it must be that $S_{\mathrm{i}} \geqslant 10.5$. Since this corresponds to a warm start, both uncertainties on the age and on the luminosity contribute to that on the minimum S_{i}, of order 0.5 k_{B}/baryon.

This lower limit on S_{i} implies that coldest-start objects of any mass are too cold by a significant 1.5–2.0 k_{B}/baryon. Various authors (e.g. Quanz et al. 2010; Bonnefoy et al. 2011) recognised that the classical cold starts (M07; Fortney et al. 2008) cannot explain the observations, but it now possible to quantify this. These results

---

[10] We note that as this manuscript was being prepared, we became aware of the first robust estimate of the bolometric luminosity, by Bonnefoy et al. (2013). They find $\log L_{\mathrm{bol}}/L_{\odot} = -3.87 \pm 0.08$, which excellently agrees with our value and thus does not change our conclusions. In particular, they find similar constraints on the initial entropy of β Pic b, although this depends on which band they use (cf. their fig. 11 with our Fig. 11).

are mostly insensitive to the uncertainty on the age range; using instead 12–22 Myr as summarised by Fernández et al. (2008) would not change the conclusions.

As for the objects in the 2M1207 and HR 8799 systems, we ran an MCMC to obtain a posterior distribution on the initial entropy. This is shown along the vertical axis of Fig. 11 for four different assumptions. In all cases, we assumed lognormal uncertainties on the age and the luminosity, with asymmetric upper and lower errorbars for the latter. For the full curve closer to the vertical axis (in blue), we applied an upper mass cut at 12 M_J and took into account that the underlying (real) mass distribution is possibly biased towards lower masses, as radial velocity measurements indicate (Cumming et al. 2008; Nielsen & Close 2010). Out of simplicity, this was done by taking the (M, S_i) distribution obtained with a flat prior in mass and multiplying it by a $dN/dM \propto M^\alpha$ prior, with $\alpha = -1.3$, thus weighing lower masses more. Of course, the value of α might depend on the formation mechanism relevant to the object but this serves to illustrate the effects of a non-constant prior on mass. The other three posterior distributions on S_i of Fig. 11 (in grey) correspond to the remaining combinations of 'with mass cut or not' and 'with power-law mass prior or not'. These curves are all similar, with the radial-velocity measurement increasing the minimum bound at half maximum from 10.2 to 10.5 k_B/baryon, quite insensitively to the use of the dN/dM prior.

At the distance from its primary where β Pic b is currently located ($\simeq$ 9 AU), core accretion is expected to be efficient and thus a likely mechanism for its formation (Lagrange et al. 2011; Bonnefoy et al. 2013). Thus, the question posed to formation models is whether core accretion can be made hotter (by 1.5–2 k_B/baryon) than what traditional cold starts predict. Since these coldest starts assume that all the accretion energy is radiated away at the shock, the constraints on the initial entropy stress the need to investigate the physics of the shock, when the initial energy content of the planet is claimed to be set.

6 SUMMARY

The entropy of a gas giant planet immediately following its formation is a key parameter that can be used to distinguish planet formation models (Marley et al. 2007). In this paper, we have explored the constraints on the initial entropy that can be obtained for directly-detected exoplanets with a measured bolometric luminosity and age. When the initial entropy is assumed to be very large, a 'hot start' evolution, the measured luminosity and age translate into a constraint on the planet mass. In contrast, when a range of initial entropies are considered ('cold starts' or 'warm starts'), the hot-start mass is in fact only a lower limit on the planet mass: larger-mass planets with lower initial entropies can also reproduce a given observed luminosity and age. Fig. 5 shows the allowed values of mass and entropy for different ages and luminosities, and can be used to quickly obtain estimates of mass and initial entropy for any given system.

To derive these constraints, we constructed a grid of gas giant models as a function of mass and central entropy which can then be stepped through to calculate the time evolution of a given planet. In a hot-start evolution, the structure and luminosity of cooling gas giant planets is usually thought of as being a function of mass and time only. Once the assumption of hot initial conditions is removed, however, a more convenient variable is the entropy of the planet. One way to think of this is that gas giants obey a Vogt–Russell theorem in which the internal structure, luminosity, and ra-

dius of a planet depend only on its mass and entropy. Fig. 2 shows the luminosity as a function of entropy for different masses, and a general fitting formula for $L(M, S)$ is given in Section 2.2. A noteworthy result is that in the intermediate-entropy regime ($S \simeq 8.5$–10 k_B/baryon), where the outer radiative zone is thick and follows a radiative-zero solution, the luminosity obeys $L = M f(S)$ as found for irradiated gas giants by Arras & Bildsten (2006), with $f(S)$ a steeply increasing function of the entropy.

We find that our models are in good agreement (within tens of percent) with the hot-start models of Burrows et al. (1997) and Baraffe et al. (2003), as well as the cold-start models of Marley et al. (2007), and cooling models calculated with the MESA stellar evolution code (Paxton et al. 2011, 2013). However, there is a small offset in the entropy of $\simeq$ 0.4 k_B/baryon between the models calculated here and using MESA on the one hand and those of Burrows et al. (1997), Baraffe et al. (2003), and Marley et al. (2007) on the other. This may be due to a difference in the implementation of the SCvH equation of state. Uncertainties due to differences in opacities or composition do not appear to be enough to account for the offset; for example, we estimate from Saumon et al. (1996) that the uncertainty in the helium (Y) and metal (Z) mass fractions introduces variations of at most 10 per cent in the luminosity.

We stress again that when the initial entropy is allowed to take a range of values, the hot-start mass is only a lower limit on the companion mass. The larger range of allowed masses means that the hot-start mass could actually lead to the mischaracterization of an object, with a hot-start mass in the planetary regime actually corresponding to an object with a mass above the deuterium-burning limit for low enough entropies. One way to break the degeneracy between mass and entropy is an accurate determination of the radius from spectral fitting (or actually a determination of $\log g$ and $T_{\rm eff}$ from the spectrum), which would yield the mass and (current) entropy of the object without any degeneracy (see e.g. Fig. 7). As discussed in Section 4, however, current atmosphere models have significant uncertainties that make this approach difficult. Another possibility is to obtain independent constraints on the mass of a companion, for example from dynamical considerations.

In Section 5, we applied our models to three directly-imaged objects which have hot-start masses in the planetary-mass regime and for some of which there are additional constraints on the planet mass. We find that the initial entropy of 2M1207 b is at least 9.2 k_B/baryon, assuming that it does not burn deuterium. For the planets of the HR 8799 system, we infer that they must have formed with $S_i > 9.2$ k_B/baryon, independent of the age uncertainties for the star. Finally, a similar analysis for β Pic b reveals that it must have formed with $S_i > 10.5$ k_B/baryon, using the radial-velocity mass upper limit of 12 M_J. These initial entropy values are respectively ca. 0.7, 0.5, and 1.5 k_B/baryon higher than the ones obtained from core accretion models by Marley et al. (2007). This quantitatively rules out the coldest starts for these objects and constrains warm starts, especially for β Pic b.

An important point is that the uncertainties in age and luminosity impact the derived hot-start mass and the lower bound on initial entropy in different ways. The major uncertainty in direct detections is the age of the star and, relevant for very young systems, all the more that of the planet. This age uncertainty translates into errorbars for the hot-start mass which are $\Delta M/M \simeq \frac{1}{2}\Delta t/t$. However, the initial entropy on the mass-independent branch of the $M(S_i)$ curve is due only to that in the bolometric luminosity, with $\Delta S_i \simeq 1/\lambda \Delta \log L_{\rm bol}$ where $\lambda \simeq 0.7$ when $S_i \lesssim 9.5$. This uncertainty

ΔS_i is typically very small, which means that, up to systematic errors, the initial entropy can be determined quite accurately.

It has been pointed out before that current direct-imaging detections are all inconsistent with the cold-start predictions from core-accretion models. It is important to stress however that the cold starts are in some sense an extreme case, as they assume complete radiation efficiency at the shock during runaway accretion, which is argued to set the low initial entropy of planet. By varying the nebula temperature or the accretion rate, Marley et al. (2007) were able to change the entropy by barely $\Delta S \simeq 0.1$, but Mordasini et al. (2012b) report that it is possible within the core-accretion scenario to obtain considerably higher entropies, increased by as much as 1–2 k_B/baryon (Mordasini et al., in prep.). With β Pic b a likely candidate for formation by core accretion, this indicates that it is essential to gain a deeper understanding about what sets the initial entropy, for instance by looking in more detail at the properties of the shock during runaway accretion.

The derived bounds on S_i for the HR 8799 objects and β Pic b made use of information on the mass, which comes from dynamical stability analyses and radial velocity, respectively. Radial-velocity data of directly-detected planets is currently available only for β Pic b, but this should change in a near future as close-in planets start being detected directly. In the absence of dynamical information, an upper limit to the mass (and thus a lower limit on the initial entropy) should be obtainable from $\log g$, even if its errorbars are large; thus, in practice, the $M(S_i)$ constraint curve does not extend to arbitrarily high masses as a pure luminosity measurement would imply.

Finally, we ran Markov Chain Monte Carlo simulations to derive more detailed quantitative constraints on the mass and entropy of directly-detected objects. When taking the uncertainties in the age and luminosity into account, we considered normal, lognormal, and flat distributions and found the chosen form to make little difference. The advantage of this approach is that it allows one to derive posterior distributions on the initial entropy, which are suitable for statistical comparisons. Given the small semi-major axis of β Pic b (9 AU), we also tried a prior $dN/dM \propto M^{-1.3}$ (which describes the population of radial-velocity planets) in addition to a flat prior on M. The latter case yielded posterior distributions on S_i with a more pronounced peak.

The benefits that the expected large increase in the number of directly-detected exoplanets in the near future should bring are at least twofold. Firstly, each new detection will yield a new constraint on the initial entropy and therefore formation mechanism. Particularly with the ability to detect lower mass gas giants at small semi-major axes ($\lesssim 20$ AU), which should be possible with instruments such as GPI or SPHERE, there will be an opportunity to constrain the state of the gas giant immediately following core accretion. Secondly, with a larger sample of objects comes a chance for a statistical comparison with formation models. For example, as noted in Section 5.1, the onset of deuterium burning leads to a relative underdensity of planets with luminosities $\sim 10^{-4}$ L$_\odot$ and ages of tens of Myrs (assuming that the masses of substellar objects are smoothly distributed near the deuterium-burning limit). Indeed, it is interesting that there appears to be such an underdensity in the current data sample (see Fig. 8), although the small number of detections so far means that this could be due to a statistical fluctuation. The best constraints on initial conditions for planet cooling will come from improved spectral models that can give reliable determinations of $\log g$ and T_{eff}.

REFERENCES

Ackerman A. S., Marley M. S., 2001, ApJ, 556, 872
Allard F., Homeier D., Freytag B., 2011, in Astronomical Society of the Pacific Conference Series, Vol. 448, 16th Cambridge Workshop on Cool Stars, Stellar Systems, and the Sun, Johns-Krull C., Browning M. K., West A. A., eds., p. 91
Allers K. N. et al., 2007, ApJ, 657, 511
Arras P., Bildsten L., 2006, ApJ, 650, 394
Baines E. K. et al., 2012, ApJ, 761, 57
Baraffe I., Chabrier G., Allard F., Hauschildt P. H., 1998, A&A, 337, 403
Baraffe I., Chabrier G., Allard F., Hauschildt P. H., 2002, A&A, 382, 563
Baraffe I., Chabrier G., Barman T., 2010, Reports on Progress in Physics, 73, 016901
Baraffe I., Chabrier G., Barman T. S., Allard F., Hauschildt P. H., 2003, A&A, 402, 701
Barman T. S., Macintosh B., Konopacky Q. M., Marois C., 2011a, ApJ, 733, 65
Barman T. S., Macintosh B., Konopacky Q. M., Marois C., 2011b, ApJ, 735, L39
Biller B. A., Close L. M., 2007, ApJ, 669, L41
Bodenheimer P., Hubickyj O., Lissauer J. J., 2000, Icarus, 143, 2
Bonnefoy M. et al., 2013, arXiv:1302.1160
Bonnefoy M. et al., 2011, A&A, 528, L15
Burrows A., Hubbard W. B., Lunine J. I., Liebert J., 2001, Reviews of Modern Physics, 73, 719
Burrows A., Liebert J., 1993, Reviews of Modern Physics, 65, 301
Burrows A. et al., 1997, ApJ, 491, 856
Callen H. B., 1985, Thermodynamics and an Introduction to Thermostatistics, 2nd edn. John Wiley & Sons, New York
Cassisi S., Potekhin A. Y., Pietrinferni A., Catelan M., Salaris M., 2007, ApJ, 661, 1094
Caughlan G. R., Fowler W. A., 1988, Atomic Data and Nuclear Data Tables, 40, 283
Chabrier G., Baraffe I., Allard F., Hauschildt P., 2000, ApJ, 542, L119
Chauvin G. et al., 2012, A&A, 542, A41
Chauvin G. et al., 2010, A&A, 509, A52
Chauvin G., Lagrange A.-M., Dumas C., Zuckerman B., Mouillet D., Song I., Beuzit J.-L., Lowrance P., 2004, A&A, 425, L29
Chauvin G., Lagrange A.-M., Dumas C., Zuckerman B., Mouillet D., Song I., Beuzit J.-L., Lowrance P., 2005, A&A, 438, L25
Close L. M., Males J. R., 2010, ApJ, 709, 342
Cox J. P., Giuli R. T., 1968, Principles of Stellar Structure. Gordon and Breach, New York
Crifo F., Vidal-Madjar A., Lallement R., Ferlet R., Gerbaldi M., 1997, A&A, 320, L29
Cumming A., Butler R. P., Marcy G. W., Vogt S. S., Wright J. T., Fischer D. A., 2008, PASP, 120, 531
Currie T. et al., 2011, ApJ, 729, 128
Currie T. et al., 2012a, ApJ, 760, L32
Currie T., Fukagawa M., Thalmann C., Matsumura S., Plavchan P., 2012b, ApJ, 755, L34
Dieterich S. B., Henry T. J., Golimowski D. A., Krist J. E., Tanner A. M., 2012, AJ, 144, 64

Ducourant C., Teixeira R., Chauvin G., Daigne G., Le Campion J.-F., Song I., Zuckerman B., 2008, A&A, 477, L1

Esposito S. et al., 2013, A&A, 549, A52

Fabrycky D. C., Murray-Clay R. A., 2010, ApJ, 710, 1408

Faherty J. K. et al., 2012, ApJ, 752, 56

Fernández D., Figueras F., Torra J., 2008, A&A, 480, 735

Fortney J. J., Hubbard W. B., 2004, ApJ, 608, 1039

Fortney J. J., Marley M. S., Hubickyj O., Bodenheimer P., Lissauer J. J., 2005, Astronomische Nachrichten, 326, 925

Fortney J. J., Marley M. S., Saumon D., Lodders K., 2008, ApJ, 683, 1104

Freedman R. S., Marley M. S., Lodders K., 2008, ApJS, 174, 504

Freistetter F., Krivov A. V., Löhne T., 2007, A&A, 466, 389

Gizis J. E., 2002, ApJ, 575, 484

Gizis J. E., Jao W.-C., Subasavage J. P., Henry T. J., 2007, ApJ, 669, L45

Golimowski D. A. et al., 2004, AJ, 127, 3516

Goździewski K., Migaszewski C., 2009, MNRAS, 397, L16

Graboske H. C., Dewitt H. E., Grossman A. S., Cooper M. S., 1973, ApJ, 181, 457

Gregory P. C., 2005, Bayesian Logical Data Analysis for the Physical Sciences: A Comparative Approach with MATHEMATICA Support. Cambridge University Press, Cambridge, UK

Grether D., Lineweaver C. H., 2006, ApJ, 640, 1051

Helling C. et al., 2008, MNRAS, 391, 1854

Hinkley S., Carpenter J. M., Ireland M. J., Kraus A. L., 2011a, ApJ, 730, L21

Hinkley S. et al., 2011b, PASP, 123, 74

Huang X., Cumming A., 2012, ApJ, 757, 47

Hubbard W. B., 1977, Icarus, 30, 305

Hubickyj O., Bodenheimer P., Lissauer J. J., 2005, Icarus, 179, 415

Ida S., Lin D. N. C., 2004, ApJ, 604, 388

Janson M., Bonavita M., Klahr H., Lafrenière D., Jayawardhana R., Zinnecker H., 2011, ApJ, 736, 89

Janson M., Carson J. C., Lafrenière D., Spiegel D. S., Bent J. R., Wong P., 2012, ApJ, 747, 116

Lafrenière D., Marois C., Doyon R., Barman T., 2009, ApJ, 694, L148

Lagrange A.-M. et al., 2012a, A&A, 542, A40

Lagrange A.-M. et al., 2011, in IAU Symposium, Vol. 276, IAU Symposium, Sozzetti A., Lattanzi M. G., Boss A. P., eds., pp. 60–63

Lagrange A.-M., De Bondt K., Meunier N., Sterzik M., Beust H., Galland F., 2012b, A&A, 542, A18

Lagrange A.-M. et al., 2009, A&A, 493, L21

Leconte J., Chabrier G., 2012, A&A, 540, A20

Liu M. C. et al., 2011, ApJ, 740, 108

Liu M. C. et al., 2010, in Society of Photo-Optical Instrumentation Engineers (SPIE) Conference Series, Vol. 7736, Society of Photo-Optical Instrumentation Engineers (SPIE) Conference Series

Lodato G., Delgado-Donate E., Clarke C. J., 2005, MNRAS, 364, L91

Lodders K., 2003, ApJ, 591, 1220

Luhman K. L., 2012, ARA&A, 50, 65

Luhman K. L., Joergens V., Lada C., Muzerolle J., Pascucci I., White R., 2007, Protostars and Planets V, 443

Malo L., Doyon R., Lafrenière D., Artigau É., Gagné J., Baron F., Riedel A., 2013, ApJ, 762, 88

Mamajek E. E., 2005, ApJ, 634, 1385

Mamajek E. E., 2012, ApJ, 754, L20

Mamajek E. E., Meyer M. R., 2007, ApJ, 668, L175

Marcy G. W., Butler R. P., 2000, PASP, 112, 137

Marley M. S., Fortney J. J., Hubickyj O., Bodenheimer P., Lissauer J. J., 2007, ApJ, 655, 541

Marley M. S., Saumon D., Cushing M., Ackerman A. S., Fortney J. J., Freedman R., 2012, ApJ, 754, 135

Marois C., Macintosh B., Barman T., Zuckerman B., Song I., Patience J., Lafrenière D., Doyon R., 2008, Science, 322, 1348

Marois C., Zuckerman B., Konopacky Q. M., Macintosh B., Barman T., 2010, Nat, 468, 1080

McBride J., Graham J. R., Macintosh B., Beckwith S. V. W., Marois C., Poyneer L. A., Wiktorowicz S. J., 2011, PASP, 123, 692

McElwain M. W. et al., 2012, in Society of Photo-Optical Instrumenta-tion Engineers (SPIE) Conference Series, Vol. 8446, Society of Photo-Optical Instrumentation Engineers (SPIE) Conference Series

Mohanty S., Basri G., Jayawardhana R., Allard F., Hauschildt P., Ardila D., 2004, ApJ, 609, 854

Mohanty S., Jayawardhana R., Basri G., 2004, ApJ, 609, 885

Mohanty S., Jayawardhana R., Huélamo N., Mamajek E., 2007, ApJ, 657, 1064

Mollière P., Mordasini C., 2012, A&A, 547, A105

Moór A., Ábrahám P., Derekas A., Kiss C., Kiss L. L., Apai D., Grady C., Henning T., 2006, ApJ, 644, 525

Mordasini C., Alibert Y., Georgy C., Dittkrist K.-M., Klahr H., Henning T., 2012a, A&A, 547, A112

Mordasini C., Alibert Y., Klahr H., Henning T., 2012b, A&A, 547, A111

Moro-Martín A., Rieke G. H., Su K. Y. L., 2010, ApJ, 721, L199

Moya A., Amado P. J., Barrado D., García Hernández A., Aberasturi M., Montesinos B., Aceituno F., 2010a, MNRAS, 405, L81

Moya A., Amado P. J., Barrado D., Hernández A. G., Aberasturi M., Montesinos B., Aceituno F., 2010b, MNRAS, 406, 566

Neuhäuser R., Schmidt T. O. B., 2012, arXiv:1201.3537

Nielsen E. L., Close L. M., 2010, ApJ, 717, 878

Patience J., King R. R., de Rosa R. J., Marois C., 2010, A&A, 517, A76

Patience J., King R. R., De Rosa R. J., Vigan A., Witte S., Rice E., Helling C., Hauschildt P., 2012, A&A, 540, A85

Paxton B., Bildsten L., Dotter A., Herwig F., Lesaffre P., Timmes F., 2011, ApJS, 192, 3

Paxton B. et al., 2013, arXiv:1301.0319

Pollack J. B., Hubickyj O., Bodenheimer P., Lissauer J. J., Podolak M., Greenzweig Y., 1996, Icarus, 124, 62

Quanz S. P. et al., 2010, ApJ, 722, L49

Reidemeister M., Krivov A. V., Schmidt T. O. B., Fiedler S., Müller S., Löhne T., Neuhäuser R., 2009, A&A, 503, 247

Riaz B., Lodato G., Stamatellos D., Gizis J. E., 2012a, MNRAS, 424, L74

Riaz B., Lodato G., Stamatellos D., Gizis J. E., 2012b, MNRAS, 422, L6

Saumon D., Chabrier G., van Horn H. M., 1995, ApJS, 99, 713

Saumon D., Guillot T., 2004, ApJ, 609, 1170

Saumon D., Hubbard W. B., Burrows A., Guillot T., Lunine J. I., Chabrier G., 1996, ApJ, 460, 993

Saumon D., Marley M. S., 2008, ApJ, 689, 1327

Schneider J., Dedieu C., Le Sidaner P., Savalle R., Zolotukhin I., 2011, A&A, 532, A79

Skemer A. J., Close L. M., Szűcs L., Apai D., Pascucci I., Biller B. A., 2011, ApJ, 732, 107

Soderblom D. R., 2010, ARA&A, 48, 581

Song I., Schneider G., Zuckerman B., Farihi J., Becklin E. E., Bessell M. S., Lowrance P., Macintosh B. A., 2006, ApJ, 652, 724

Spiegel D. S., Burrows A., 2012, ApJ, 745, 174

Spiegel D. S., Burrows A., Milsom J. A., 2011, ApJ, 727, 57

Stelzer B., Scholz A., Jayawardhana R., 2007, ApJ, 671, 842

Stephens D. C. et al., 2009, ApJ, 702, 154

Stevenson D. J., 1979, MNRAS, 187, 129

Stevenson D. J., 1982, Planet Space Sci., 30, 755

Su K. Y. L. et al., 2009, ApJ, 705, 314

Sudol J. J., Haghighipour N., 2012, ApJ, 755, 38

van Leeuwen F., 2007, A&A, 474, 653

Vigan A., Moutou C., Langlois M., Allard F., Boccaletti A., Carbillet M., Mouillet D., Smith I., 2010, MNRAS, 407, 71

Zapolsky H. S., Salpeter E. E., 1969, ApJ, 158, 809

Zuckerman B., Song I., Bessell M. S., Webb R. A., 2001, ApJ, 562, L87

APPENDIX A: AGE, LUMINOSITY, AND MASS CONSTRAINTS

A1   2M1207

A1.1   Age and luminosity

The first directly-imaged object with a hot-start planetary mass (Chauvin et al. 2004, 2005) is located $0.8''$ from its M8 brown-dwarf primary, a well-studied (see Gizis 2002 for the discovery paper and Skemer et al. 2011 for a summary) member of the young (8^{+4}_{-3} Myr) TW Hydræ association (Chauvin et al. 2004; Song et al. 2006) at a distance of 53 ± 1 pc (as averaged by Skemer et al. 2011 from Gizis 2002; Gizis et al. 2007; Biller & Close 2007; Mamajek 2005; Mamajek & Meyer 2007; Ducourant et al. 2008), implying a projected orbital separation of 41 ± 1 AU.

Determining the luminosity of 2M1207 b is not straightforward. Photometry is available in the *J* Mohanty et al. (2007), *H*, K_s, and *L'* bands from NaCo observations at the VLT (Chauvin et al. 2004; Mohanty et al. 2007), at 0.8–1.0, 1.0–1.2, 1.35–1.55, and 1.4–1.8 μm (similar to *H*) from the *Hubble Space Telescope* (Song et al. 2006), and in the *Herschel* SPIRE bands of 250 and 350 μm Riaz et al. (2012b,a). Skemer et al. (2011) also obtained an upper limit at 8.3–9.1 μm. Spectroscopy is available at 1.1–1.35 μm, 1.4–1.8 μm (Chauvin et al. 2004; Mohanty et al. 2007; Patience et al. 2010), and 1.95–2.5 μm (Patience et al. 2010) and 2.0–2.4 μm (Mohanty et al. 2007), i.e. in JHK_s and slightly redward. Summing up the fluxes in *J*, *H*, K_s, and *L'* listed in Mohanty et al. (2007) and using the known distance gives a luminosity of 2.1×10^{28} erg s^{-1}, or 27–30 per cent of a bolometric luminosity $\log L_{bol}/L_\odot = -4.68$ to -4.74 (see below). A 'direct luminosity determination' is thus not possible.

As summarised by Barman et al. (2011b), there are inconsistencies between the luminosity of 2M1207 b and its spectral type, determined by Chauvin et al. (2004) to be L5–L9.5. With the corresponding bolometric correction BC_K of Golimowski et al. (2004), the K_s-band magnitude implies a luminosity of $\log L/L_\odot = -4.7 \pm 0.1$ (Barman et al. 2011b). The hot-start, equilibrium models of Baraffe et al. (2003) then yield from the age and luminosity an effective temperature of 1010 ± 80 K (Barman et al. 2011b) in disagreement with $T_{eff} \simeq 1600$ K implied by the spectral type (Mohanty et al. 2007; Patience et al. 2010, 2012). However, this second value is questionable. Indeed, the high effective temperature and low luminosity would require an improbably small radius of $\simeq 0.6$ R$_J$.

There are two distinct approaches to the solution. Mohanty et al. (2007) argue that the actual luminosity has been underestimated due to grey extinction by an almost edge-on disc (the $\simeq 25$-M$_J$ brown-dwarf primary is accreting; e.g. Stelzer, Scholz, & Jayawardhana 2007). The correspondingly higher luminosity is reported by Ducourant et al. (2008) as $\log L_{bol}/L_\odot = -3.8 \pm 0.1$. On the contrary, Skemer et al. (2011) argue against the disc explanation and suggest that thicker clouds than what might be naïvely expected[11] are needed. Barman et al. (2011a,b) go further and explicitly claim that the problem is with the derived T_{eff}. They show that an atmosphere model with $T_{eff} = 1000$ K can fit very well the photometry and spectroscopy if clouds of typical thickness and also, crucially, non-equilibrium chemisty are included. The latter leads to a heavily reduced methane abundance (by ca. two orders of magnitude at photospheric depths) compared to the chemical-equilibrium clouds and thus to redder colours than expected. From their best-fitting models, Barman et al. (2011b) estimate a luminosity of $\log L/L_\odot = -4.68 \pm 0.05$, in agreement with the luminosity derived from BC_K. As Luhman (2012) notes, differing bolometric corrections for old (field) and young brown dwarfs are thus not the sole explanation.

We adopt the luminosity of Barman et al. (2011b), in agreement with Neuhäuser & Schmidt (2012) who report $\log L/L_\odot = -4.74 \pm 0.06$ (with however $T_{eff} = 1590 \pm 280$ K). Using the age of 5–12 Myr and the Baraffe et al. (2003) cooling tracks, this luminosity yields a hot-start mass of 2–5 M$_J$ as Barman et al. (2011b) state. Skemer et al. (2011) give a slightly higher hot-start mass between 5 and 7 M$_J$ based on $T_{eff} = 1000$ K

---

[11] See comment in section 1.2.2 of Marley et al. (2012).

and the Burrows et al. (1997) models. We note that these errorbars match the estimate $\Delta M/M \simeq \frac{1}{2}\Delta t/t \simeq 0.5$ from Section 3.1.

A1.2   Mass information

Mass information of dynamical origin for this two-body system is not available. Indeed, since the separation implies a period of at least (depending on the eccentricity) 1700 yr, detectable orbital evolution or change of the velocity amplitude are not expected in the near future (Mamajek 2005), precluding both astrometry and radial-velocity measurements.

However, the surface gravity is somewhat constrained, which can be used to set an approximate mass upper limit. Barman et al. (2011b) state that their best-fitting model has $g = 10^4$ cm s^{-2} but do not provide any sense of how large the uncertainty on this value might be. However, typical errorbars (as in their similar analysis for HR 8799 b; Barman et al. 2011a) are at least of 0.5 dex. Mohanty et al. (2007) found that the fit to both the photometric and spectroscopic data is rather insensitive to $\log g$ within 3.5–4.5 (cm s^{-2}), in agreement with the indications of low gravity from the triangular *H*-band spectral shape and relatively weak Na ɪ absorption (e.g. Allers et al. 2007; Mohanty et al. 2007). Also, Patience et al. (2012) fit *J*, *H*, and *K* spectra with five grids of atmosphere models, including BT-*Settl* (Allard, Homeier, & Freytag 2011), *Drift*-ᴘʜᴏᴇɴɪx (Helling et al. 2008), and those of Marley et al. (Ackerman & Marley 2001). The Marley et al. models yielded a gravity on the edge of their grid ($g = 10^{5.0}$ cm s^{-2}), but the others gave $\log g \simeq 3.5, 3.5, 4.3$, and 5.0 (cm s^{-2}), respectively. (With the best-fitting $T_{eff} = 1500$–1650 K, the implied radii are of 0.4–0.7 R$_J$, well below any theoretical cooling track.) Even though there are systematic issues with atmosphere models of young, low-mass brown dwarfs are expected, we will take these results to suggest tentatively that 2M 1207 b has a low gravity. As discussed below, the initial entropy on the cold-start branch is $S_i = 9.2$, which is thus an *upper* limit to the current entropy. With $S < 9.2$ and a reasonable upper limit $\log g < 4.0$ (cm s^{-2}), the upper bound on the mass is $\simeq 7$ M$_J$, and for $\log g = 4.35$ (cm s^{-2}) it is 12.7 M$_J$. Therefore, we shall assume that the estimates of the surface gravity imply a mass below the deuterium-burning limit, which is near 13 M$_J$ (Spiegel et al. 2011).

A2   HR 8799

A2.1   Age and luminosities

Several properties of HR 8799 let its age be estimated: variability from non-radial oscillations, low abundance of iron-peak elements, and far-IR excess due to circumstellar dust (Marois et al. 2008). Along with its Galactic space motion and position in a Hertzsprung–Russell diagram, these let Marois et al. (2008) estimate an age range of 30–160 Myr with a preferred value of 60 Myr, consistent with the 20–150 Myr range of Moór et al. (2006) based on membership in the Local Association. Recently, Baines et al. (2012) used interferometric measurements of HR 8799's radius to derive a stellar mass and age. They found best-fitting ages of 33 or 90 Myr, depending on whether the star is approaching or moving away from the main sequence. However, the statistical errorbars, which do not take uncertainties in the stellar models into account, are considerable in the second case (the 1-σ ranges are 20–40 and 40–471 Myr, respectively). Nevertheless, if Baines et al.'s measurement of the stellar radius and the deduced metallicity are correct, the age range of 1.1–1.6 Gyr from the asteroseismological analysis of Moya et al. (2010a) would be compromised, as Baines et al. (2012) point out. Indeed, they estimate a near-solar metallicity, which contrasts with the [M/H] $\simeq -0.3$ or -0.1 result of Moya et al. (2010b), while metallicity is an important input of asteroseismological analyses. Moreover, there is the statistical argument put forth by Marois et al. (2008) that massive discs (such as HR 8799's of 0.1 $M_\oplus$; Su et al. 2009) are unlikely to be found around older stars. In our analysis, we shall therefore ignore the 1.1 Gyr result and instead use 20 and 160 Myr as lower and upper limits, which brackets the ranges reviewed in Moya et al. (2010a) and Baines et al. (2012).

Marois et al. (2008, 2010) estimated luminosities of $\log L_{bol}/L_\odot = -5.1 \pm 0.1$ (HR 8799 b), -4.7 ± 0.1 (cd) and -4.7 ± 0.2 (e) from the known

distance of 39.4 ± 0.1 pc and six infrared magnitudes, covering $\simeq 40$ per cent of the bolometric luminosity, and also from bolometric corrections for brown dwarfs. For their part, Marley et al. (2012) recently derived luminosities of $\log L_{\rm bol}/L_\odot = -4.95 \pm 0.06, -4.90 \pm 0.10$, and -4.80 ± 0.09 for planets b, c[12], and d, respectively, by self-consistently obtaining the radius from evolutionary models. This contrasts with the usual procedure of optimising $(R/d)^2$ along with $T_{\rm eff}$ and $\log g$ to fit the photometry, which yields unphysically small radii of $\simeq 0.8$ $R_{\rm J}$ (Barman et al. 2011a; Marley et al. 2012). Since Marley et al. considered only hot starts, i.e. fixed $S_{\rm i}$ = high, the cooling tracks are $L_{\rm bol}(M, t)$ and $R(M, t)$ relations, which let R and t be uniquely determined from $\log g$ and $T_{\rm eff}$. This gives an age of 360 Myr for HR 8799 b and age ranges of 40–100 Myr and 30–100 Myr for c and d, consistent with other literature estimates. Given the difficulties in obtaining a reasonable fit, Marley et al. (2012) warn that the first result should not be taken seriously, and note that the tension in the age would be reduced by considering colder initial conditions. In our analysis, the luminosity values of Marois et al. (2008, 2010) will be used since they are standard and almost or marginally consistent with those of Marley et al. (2012).

Finally, an age of 30 or 60 Myr for the system lead Marois et al. (2010) to derive from the luminosity and the cooling tracks of Baraffe et al. (2003) masses of $(5, 7, 7, 7)$ or $(7, 10, 10, 10)$ $M_{\rm J}$. The uncertainty in the age implies (see Section 3) $\Delta M \simeq 1$–1.3 $M_{\rm J}$ for the hot-start values.

A2.2 Dynamical stability

Since it is to date the only directly-imaged multiple-planet system, HR 8799 has received a considerable amount of attention with regard to its dynamical stability (e.g. Marois et al. 2008; Reidemeister et al. 2009; Fabrycky & Murray-Clay 2010; Moro-Martín et al. 2010; Marois et al. 2010; Currie et al. 2011; Sudol & Haghighipour 2012; Esposito et al. 2013; Currie et al. 2012b; see review in Sudol & Haghighipour 2012). However, only the most recent studies were able to consider all four planets. Crucial questions include whether there are two- or three-planet mean-motion resonances (as Goździewski & Migaszewski 2009 and Fabrycky & Murray-Clay 2010 suggest), what the inclination and eccentricities of the orbits are (for instance, Lafrenière et al. 2009 estimated 13–23° for the inclination of HR 8799 b with respect to the plane of the sky) and whether they are co-planar (against which Currie et al. 2012b recently provided evidence), and, naturally, what the masses (including that of the star) are and how long the system should be required to survive. Solutions are very sensitive to these parameters and even to the numerical integrator used, as Esposito et al. (2013) note. The parameter space's high dimensionality makes a proper exploration – i.e. without artificially-imposed restrictions as all authors had to assume –, computationally prohibitive, and trying to include information about the disc would only make matters worse.

Stability is estimated by using astrometric constraints and numerically evolving the system over time, requiring that it be stable (without collisions nor ejections) for a period equal to its age. However, Goździewski & Migaszewski (2009) and Fabrycky & Murray-Clay (2010) point out that if it is young with respect to its main-sequence lifetime, HR 8799 could indeed be a transient system undergoing dynamical relaxation. Therefore, it may not be possible to draw firm conclusions even from the results of a complete analysis.

Nevertheless, if the direction in which these studies point is correct, the planets should have as low masses as allowed, with however higher masses permitted if some orbits are resonant. For this reason, we shall consider as approximate upper masses from stability analyses 7, 10, 10, and 10 $M_{\rm J}$ for HR 8799 b, c, d, and e, respectively. In particular, while the opposite cannot be solidly excluded, it seems plausible that none is a deuterium-burning object.

A3 β Pic

A3.1 Age and luminosity

The namesake A5 dwarf of the nearby (9–73 pc; Malo et al. 2013) β Pictoris moving group has an age of 12^{+8}_{-4} Myr (Zuckerman et al. 2001) and asymmetric outer and warped inner discs, which have been observed for more than two decades (Lagrange et al. 2009, 2012a, see review in Lagrange et al. 2011). A companion was first detected in L' (Lagrange et al. 2009) and subsequently confirmed at 4 μm (Quanz et al. 2010) and in K_s (Bonnefoy et al. 2011). Very recently, Bonnefoy et al. (2013) added to these observations photometry in J, H, and M'. The distance of 19.44 ± 0.05 pc[13] to β Pic b implies an orbital separation of 8–9 AU (Chauvin et al. 2012; Bonnefoy et al. 2013), which is the smallest of all low-mass directly-detected objects. An object at this position had been predicted from the disc morphology by Freistetter, Krivov, & Löhne (2007).

Until recently, the only bolometric luminosity estimate for β Pic b is due to Neuhäuser & Schmidt (2012), who report $\log L_{\rm bol}/L_\odot = -3.90^{+0.07}_{-0.40}$. They firstly derived, from the $T_{\rm eff} = 1700 \pm 300$ K value of Bonnefoy et al. (2011), a spectral type SpT $\simeq$ L2–T4 using the $T_{\rm eff}$–SpT relation of Golimowski et al. (2004, hereafter G04). They then estimated from their SpT–BC_K curve a bolometric correction $BC_K = 3.3^{+0.15}_{-1.00}$ (T. Schmidt, priv. comm.). Thus, the large, asymmetric lower errorbar on the luminosity comes from the large, asymmetric lower errorbar on the bolometric correction, which itself is due to the flat $T_{\rm eff}$–SpT relation between L7 and T4 in G04. A more direct approach to the bolometric luminosity consists of converting the colour to a spectral type and obtaining from this a bolometric correction. Also using the fits of G04, this gives the same luminosity as found by Neuhäuser & Schmidt (2012) but with a smaller lower errorbar of 0.12 dex. One should however note that BC_K(SpT) is not a monotonic function (see fig. 6a of G04), so that the errorbars are strongly non-Gaußian. With a maximum BC_K of 3.3 mag near L4, $\log L_{\rm bol}/L_\odot$ cannot formally be above -3.9 dex. However, the BC_K–SpT relation of G04 was derived for field dwarfs (see also Stephens et al. 2009), and the spectral classification of young objects is not yet well understood nor, in fact, well defined (see e.g. Liu et al. 2011; Faherty et al. 2012). Keeping in mind these uncertainties in interpreting the photometry, we shall use for the analysis $\log L_{\rm bol}/L_\odot = -3.90^{+0.05}_{-0.12}$, where the upper errorbar reflects the residuals of the G04 fit.

A3.2 Mass information

The object β Pic b is particularly interesting because it is the first directly-imaged companion for which radial-velocity (RV) data is also available[14] (Lagrange et al. 2012b). Using new and archival data spanning eight years and thanks to the high inclination of the system ($88 \pm 2°$; Chauvin et al. 2012), Lagrange et al. (2012b) were able to place tentative lower mass limits of 1–2 $M_{\rm J}$, which is fully consistent with all reasonable age and luminosity combinations, even allowing for very large lower errorbars on the latter. However, Lagrange et al.'s upper limit of 10–25 $M_{\rm J}$, with 12 $M_{\rm J}$ for the most probable orbit of 9 AU (Lagrange et al. 2009; Chauvin et al. 2012) is an important result which excludes high-mass solutions and puts the object quite likely in the planetary (non-deuterium burning) range.

---

[12] In fact, the errorbars on the luminosity of HR 8799 c are clearly non-Gaußian, but this will not be taken into account out of simplicity.

[13] This is the value obtained from a re-reduction of *Hipparcos* data by van Leeuwen (2007). However, a number of recent studies still use the value of 19.3 ± 0.2 pc (Crifo et al. 1997).

[14] To this rarity contribute both intrinsic detection biases – direct imaging favours planets further out from their star, resulting in a small RV signal – as well as selection biases – target stars are usually chosen based on the presence of a disc, which implies that the systems are preferentially seen face-on. A possible further hindrance is that young stars – young systems being of more interest – are usually active and thus less amenable to radial-velocity measurements.